DISSERTATION

SIMPLE ANALYTICAL SOLUTIONS FOR POTENTIAL VORTICITY INTRUSIONS

Submitted by

Matthew Thomas Masarik

Department of Atmospheric Science

In partial fulfillment of the requirements

for the Degree of Doctor of Philosophy

Colorado State University

Fort Collins, Colorado

Summer 2012

Doctoral Committee:

Advisor: Wayne H. Schubert

Richard E. Eykholt
Eric D. Maloney
David A. Randall

ABSTRACT

SIMPLE ANALYTICAL SOLUTIONS FOR POTENTIAL VORTICITY INTRUSIONS

Using potential temperature (θ) as the vertical coordinate, we derive analytical solutions of the potential vorticity (PV) invertibility principle for the case in which the flow is y-independent and an isolated PV anomaly is confined within an ellipse in the (x, θ)-plane. The solutions aid in understanding the dynamics of low latitude PV intrusions whose associated cloud patterns are often referred to as moisture bursts, or tropical plumes and whose flow patterns are often referred to as tropical upper tropospheric troughs (TUTTs). The solutions illustrate the phenomenon of isentropic upglide below an upper tropospheric positive anomaly in PV. They also quantify how the partitioning of PV between vorticity and static stability depends on the shape and strength of the PV anomaly. The solutions also apply to the problem of determining the balanced flow induced by a surface temperature anomaly, which is equivalent to a very thin layer of infinite PV at the surface. Reanalysis data is consulted as a check on the solutions. Finally, a numerical model is constructed where approximations made in the analytical theory can be examined.

ACKNOWLEDGEMENTS

I would like thank the Schubert Research Group, Brian McNoldy for generation of IDL figures, Paul Ciesielski for assistance with GrADS and the YOTC data set, Rick Taft for help troubleshooting many computing related issues, and Levi Silvers for help with the numerical modelling chapter. I would like to thank my committee: Dr. Richard Eykholt, Dr. Eric Maloney, and Dr. Dave Randall for their time and insight on this project. I would like to thank my advisor, Dr. Wayne Schubert for his guidance and support during this process. Research support has been provided by the National Science Foundation under Grant ATM-0837932 and under the Science and Technology Center for Multi-Scale Modeling of Atmospheric Processes, managed by Colorado State University through cooperative agreement No. ATM-0425247.

TABLE OF CONTENTS

Chapter 1

INTRODUCTION

Figure 1.1 is an infrared image of a tropical plume over the eastern North Atlantic and northwest Africa. Superimposed on the cloud field are streamlines and isotachs at the 345 K isentropic surface. On the southeast side of the trough there is a long plume of cloudiness, along with southwesterly winds with speeds ranging between 40 and 70 m s^{-1}. Cloud patterns like this (reviewed by Knippertz, 2007) go by a variety of other names, such as cloud surges, moisture bursts (McGuirk et al., 1987), and tropical upper tropospheric moisture (Newell et al., 1997). The flow patterns are often referred to as tropical upper tropospheric troughs (TUTTs), and the signatures in the potential vorticity (PV) field as stratospheric intrusions (Appenzeller and Davies, 1992; Appenzeller et al., 1996), and low-latitude PV intrusions (Funatsu and Waugh, 2008). Early work by Sadler (1976, 1978), looked at TUTTs and their role in tropical cyclone development in the western Pacific. More recently, upper tropospheric PV anomalies over the Atlantic basin have been implicated in the development of tropical cyclones from extratropical precursors in a process known as tropical transition (TT) (Davis and Bosart, 2004).

While such flow patterns can apparently occur at any longitude, they seem to occur frequently in the eastern Pacific. In the boreal fall, winter, and spring the upper troposphere in the eastern Pacific differs from most of the tropical belt in the sense that it contains westerly rather than easterly winds. This background westerly flow is favorable for the equatorward propagation of mid-latitude Rossby waves (Hoskins and Ambrizzi, 1993), which have been linked to modulation of tropical convection in the ITCZ region (Kiladis and

Weickmann, 1992; Kiladis, 1998).

Climatologies of the intrusions of extratropical air into the tropical upper troposphere have been produced by Postel and Hitchman (1999), Waugh and Polvani (2000), and Waugh and Funatsu (2003). These studies show that, in the eastern Pacific, such events produce narrow tongues of high PV that have an almost north-south orientation and last approximately three days.

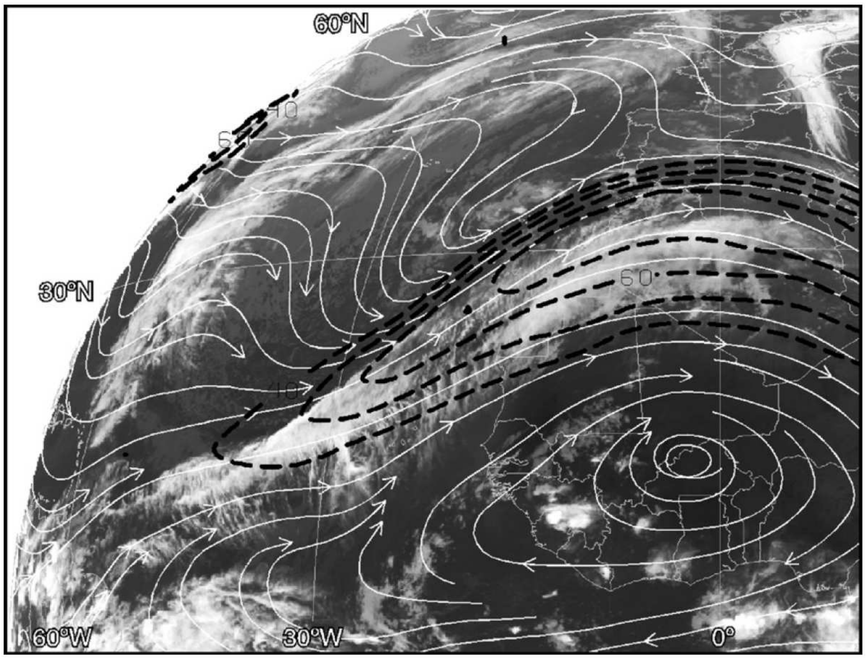

Figure 1.1: Infrared image of a tropical plume over the eastern North Atlantic and northwest Africa at 00 UTC on 31 March 2002. The solid lines and dashed lines are streamlines and isotachs on the 345 K isentropic surface, with dashed isotachs indicating 40, 50, 60, and 70 m s^{-1}. Adapted from Knippertz (2007).

Knippertz (2007) adapted Fig. 1.2 from Waugh and Funatsu (2003) who used 20 years of NCEP-NCAR reanalysis data to study intrusions into the upper troposphere and the associated OLR and ozone signatures. To examine the relationship between PV intrusions into low latitudes and tropical convection, composite PV and OLR fields were constructed. This was done by phase-shifting all intrusion events identified on the 350 K isentrope, then averaging. First, composites were made based on the definition of high PV intrusion events. From the resulting PV and OLR fields it was found that when there is an intrusion event, there is nearly always low OLR. To test the converse, composites of PV and OLR were constructed based on defined “low OLR” events. The results of these composites were weaker but similar, making the case that transient convection and high PV intrusions into the central and eastern northern Pacific nearly always occur together.

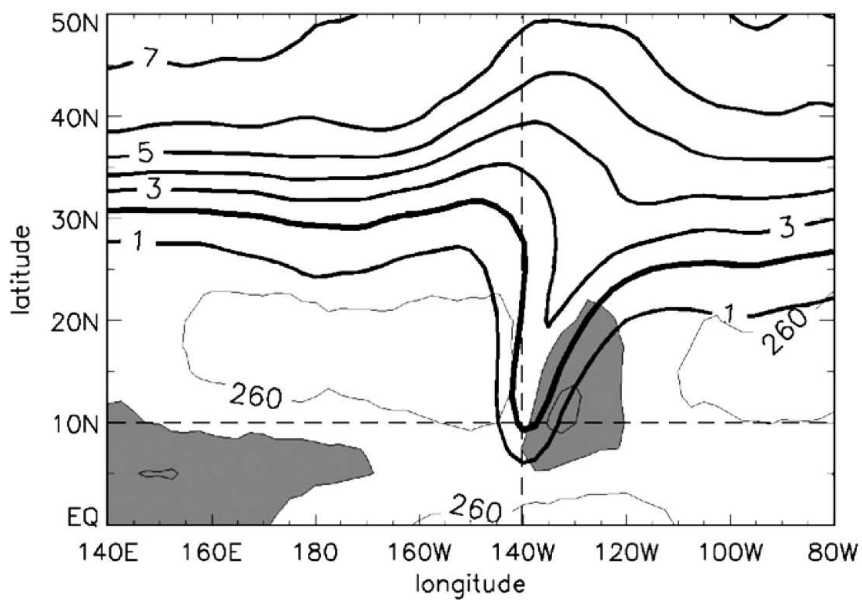

Figure 1.2: Composite low-latitude PV intrusion (the thick contours are labeled in PV units) over the North Pacific on the 350 K isentropic surface. The thin contours show the outgoing longwave radiation (OLR) with the shaded regions indicating values less than 240 W m^{-2}, which is typical of tropical convection. The tropical convection just east of the high PV intrusion is associated with the isentropic upglide process. Adapted from Waugh and Funatsu (2003).

Figure 1.3 shows the Special Sensor Microwave/Imager (SSM/I) water vapor product for a 12 hour period on 7 January 2009 over the north Pacific Basin. A long, narrow band of enhanced water vapor can be seen extending from the subtropics near the dateline and making landfall on the Washington coast. Over the period 6-8 January, western Washington experienced a major atmospheric river event with rainfall totals of 3-8 inches (ESRL/PSD, 2012), which, combined with melting snow and saturated soils, led to flooding (Neiman et al., 2011) of several river basins. The top panel of Fig. 1.4 shows the 250 hPa potential vorticity for 18Z on 7 January 2009. Just off the coast of North America a Rossby wave breaking event in its early stages is seen. Referring back to Fig. 1.3, the location of this breaking wave is seen to be just north-west of the elongated band of high water vapor content. The thick black line at 45° N indicates the location of the vertical cross-section displayed in the lower panel of Fig. 1.4. In the cross-section, a region of stratospheric air having PV values ∼7 PVU's can be seen protruding downward into the upper troposphere. On the east side of this anomly there is isentropic upgliding, as well as a strong northward jet with speeds of 50 m s^{-1} in the core.

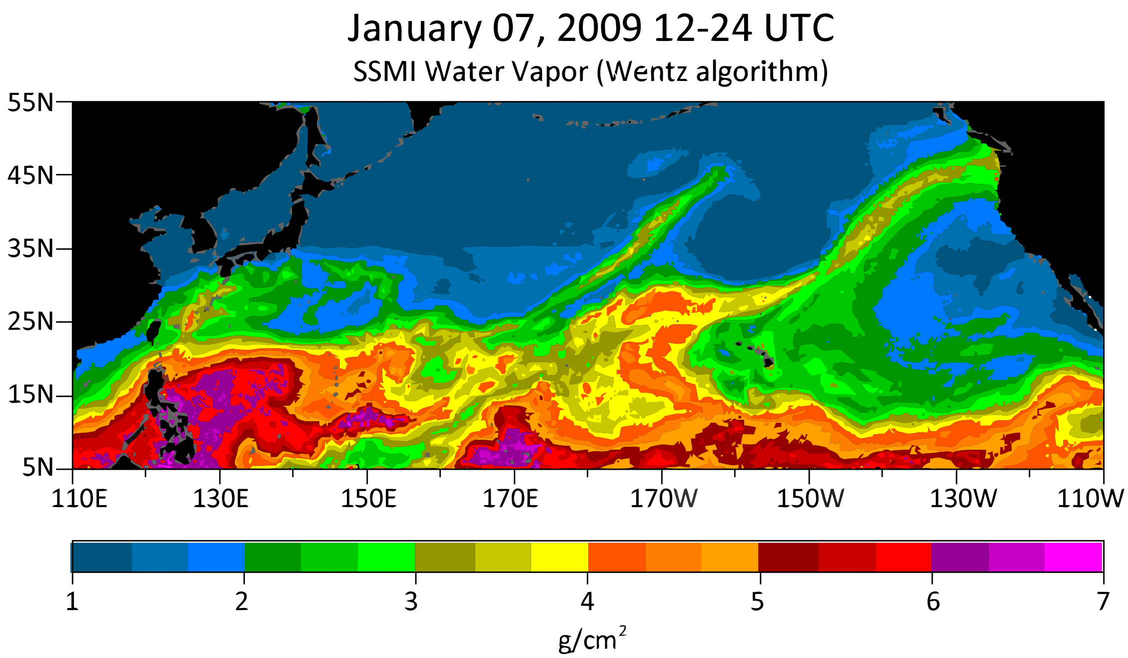

Figure 1.3: SSM/I water vapor image for the period 12-24 UTC on 07 January 2009. During this time an atmospheric river event affected the Washington coast. The colorbar indicates column water vapor concentrations in g cm^{-2}. Image courtesy of ESRL/PSD Atmospheric River Information Page.

Above we introduced some important meteorological events (e.g., TUTTS, tropical convection, tropical cyclone development, atmospheric rivers) associated with intrusions of potential vorticity into the upper troposphere. The goal of this work is to better understand the dynamics of PV intrusions through the derivation of simple analytical solutions of the PV invertibility principle. One thing to note about these solutions is that they apply

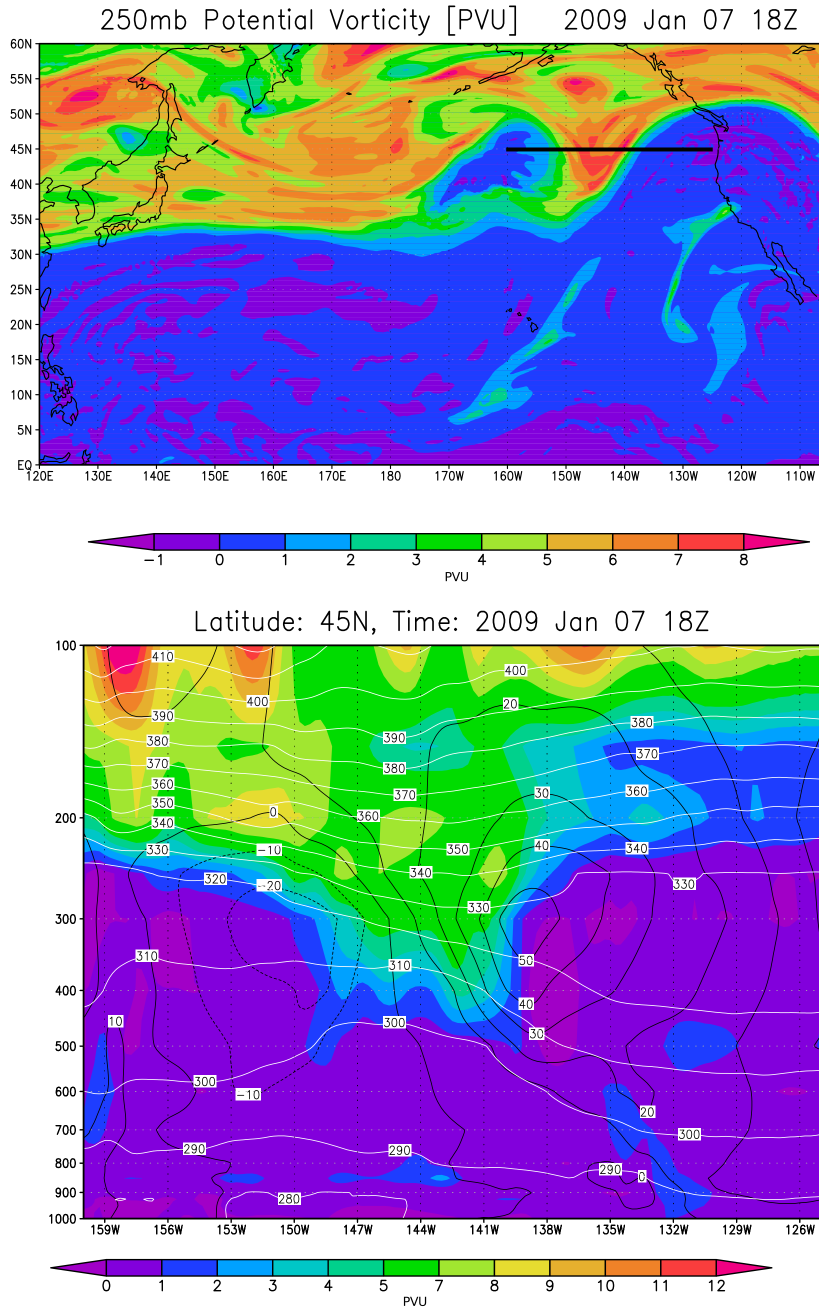

Figure 1.4: The top panel shows potential vorticity on the 250mb surface at 18Z on 07 January 2009. The thick black line indicates the location of the vertical cross-section shown in the lower panel. The lower panel shows potential vorticity (PV, colors), wind speed (v, solid and dashed black lines every 10 ms^{-1}), and potential temperature (θ, white lines every 10 K). For both panels the respective colorbar indicates PV values in PVU's.

not only to intrusions of high PV, but also to the case of low PV air protruding into a region of higher PV air. The organization is as follows. Chapter 2 is an observational survey. Reanalysis data from the 'Year' Of Tropical Convection (YOTC) data set is used to look for PV intrusion events. We identify one event for each type of intrusion and then further examine it by taking cross-sections of its vertical structure. In the cross-sections the potential vorticity in PV units (or PVU's where 1 PVU $= 1.0 \times 10^{-6}$ $\mathrm{m^2 s^{-1} K\ kg^{-1}}$) is displayed, as well isentropes and meridional wind for north-south oriented intrusions.

Chapter 3 is the focus of this work. The starting point is with the primitive equations in physical height coordinates from which we derive a set of equations in θ-coordinates governing y-independent flow in geostrophic balance. From here the potential vorticity invertibility relation is found, which is in the form of Cauchy-Riemann equations. Solving these for an isolated PV anomaly yields simple analytical solutions. Further, these solutions are then used to partition the potential vorticity into the components of vorticity and static stability.

In Chapter 4, a numerical study, the full unapproximated equations from the analytical section are numerically integrated. Two particular approximations are investigated: the approximation of the density by the far-field density, as well as the exclusion of a stratosphere.

Conclusions and suggestions for future work are given in Chapter 5.

Chapter 2

OBSERVATIONAL SURVEY

The goal of the observational survey is to identify potential vorticity intrusions in the data and analyze the characteristics of the flow induced by the intrusions. The data used is from the 'Year' Of Tropical Convection (YOTC) data set, which consists of two years of European Centre for Medium-Range Weather Forecasts (ECMWF) reanalysis fields from 1 May 2008 to 30 April 2010. Because the features we would like to resolve can be as narrow as O(200 km) (Appenzeller and Davies, 1992), data with a high degree of horizontal resolution was needed. The data was available on a latitude/longitude grid having $0.25° \times 0.25°$ resolution, and at 15 pressure levels between the surface and 100 hPa.

Waugh and Polvani (2000) found that intrusion events occurred almost exclusively within "westerly ducts", which are a characteristic of the upper tropospheric equatorial westerly winds found over the Pacific Ocean during northern fall to spring. Based on this, time series maps of potential vorticity on the 250 hPa surface were created for the Northern Hemisphere winter months (December, January, and February). We looked then looked for instances where air having high values of potential vorticity pushed southward into an air mass having lower values of PV. We also looked at the opposite case, when an air mass having lower values of potential vorticity pushes northward into a region of higher PV. One event for each of these cases was singled out for further examination.

2.1 Southward intrusions of high PV

The first event started around 10 January 2009 and lasted nearly a week. The time series for this event is shown in Figs. 2.1 and 2.2. At 00Z on 10 January 2009 a wave in the 250 mb potential vorticity field is starting to develop at 180° and 30° N. Over the next 36 hours the intrusion pushes southward and has elevated values of PV at its tip, between 15°-20° N. At 00Z on 12 January the intrusion starts to weaken and become a filament and by 12Z a vortex is seen to have developed within the filament just north of Hawaii. These "subfilament" scale structures were identified by Scott et al. (2001) and studied via a nonhydrostatic mesoscale model as well as the technique of Contour Advection with Surgery (CAS), developed by Dritschel (1989). This mesoscale structure of filaments was also observed by Appenzeller et al. (1996), who in addition produced a schematic of archetypal PV streamer patterns. The intrusion of our focus can be identified as a Type II streamer, with the remnants of a decaying intrusion to the east being a Type I streamer. During the next two days the intrusion continues to stretch out along its axis and by this point has reached as low as 10° N. At 12Z on 16 January the filament starts to strengthen and grow slightly in width, which continues to 00Z on 17 January. On January 17 at 12Z the tip is seen to start to curve in on itself. Beyond here the filament continues to move eastward and makes landfall on the west coast of North America. A vertical cross-section of this event, early in its development at 06Z on 11 January 2009, is shown in Fig. 2.3. The top panel of Fig. 2.3 shows the intrusion with its tip at 20° N and having values near 7-8 PVU along much of its length. The heavy black line indicates the location of the cross-section taken at 30° N from 180°-150° W. The lower panel shows a vertical cross-section of potential vorticity, meridional wind, and potential temperature surfaces. There is a region of anomalously high PV protruding downward into the troposphere, reaching as far as 600 hPa with $\sim$2 PVU's and having values of 7-8 PVU's in its core. Flanking the sides of the anomaly are jets which have a high degree of symmetry in both shape and magnitude. These circulation anomalies reach their maximum on the edges of the PV anomaly. On the right

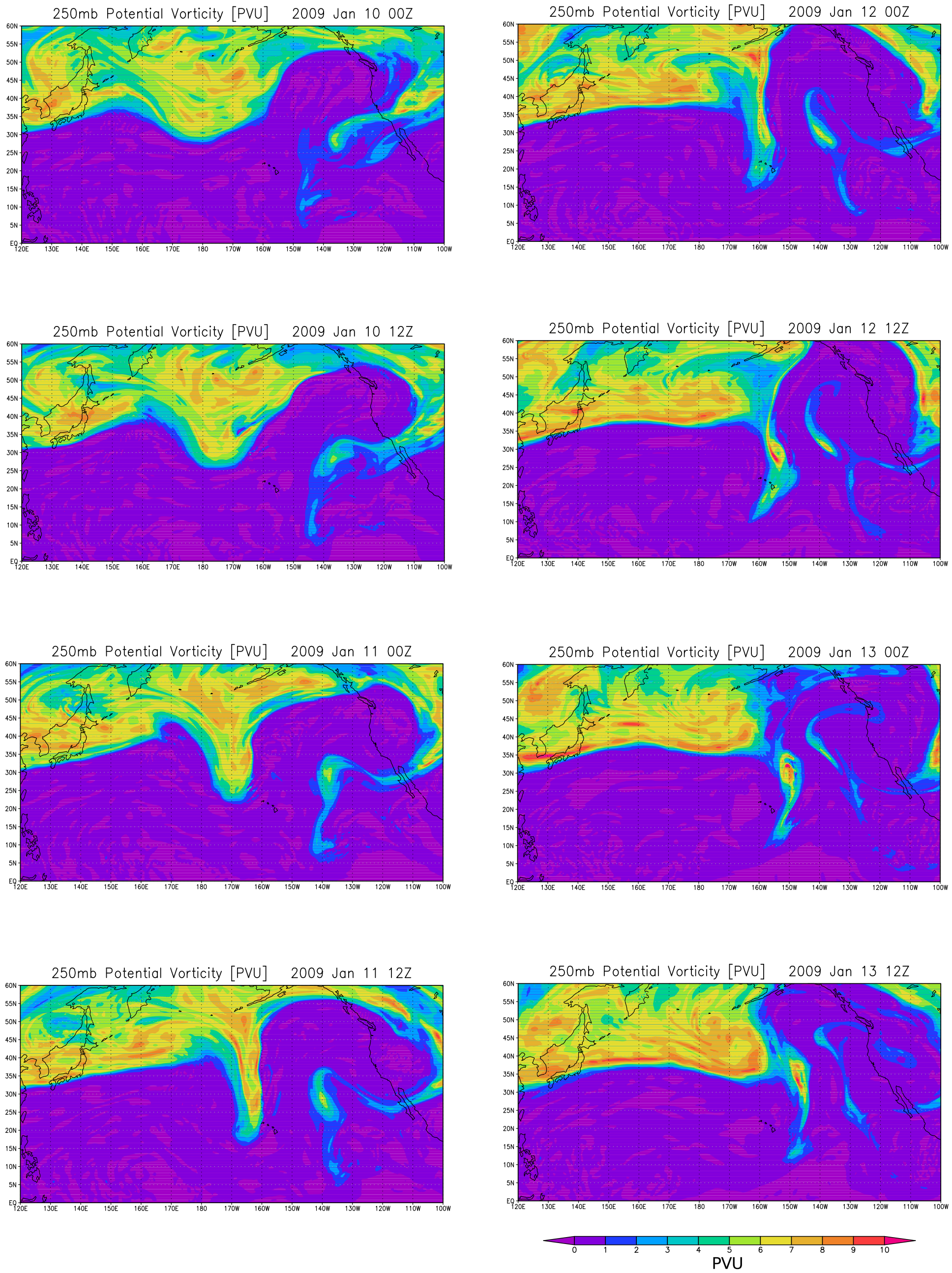

Figure 2.1: Time series of potential vorticity (PV) on the 250 hPa surface shown every 12 hours starting at 00Z on 10 January 2009. This figure contains the first half of the lifecycle of a high PV intrusion. The second half is shown in Fig. 2.2. The colorbar at the bottom indicates the values of PV in PVU's.

side the northward wind has a maximum of 60 m s^{-1} and on the left side a small core reaches a minimum of -70 m s^{-1}. Underneath the anomaly the surfaces of potential temperature

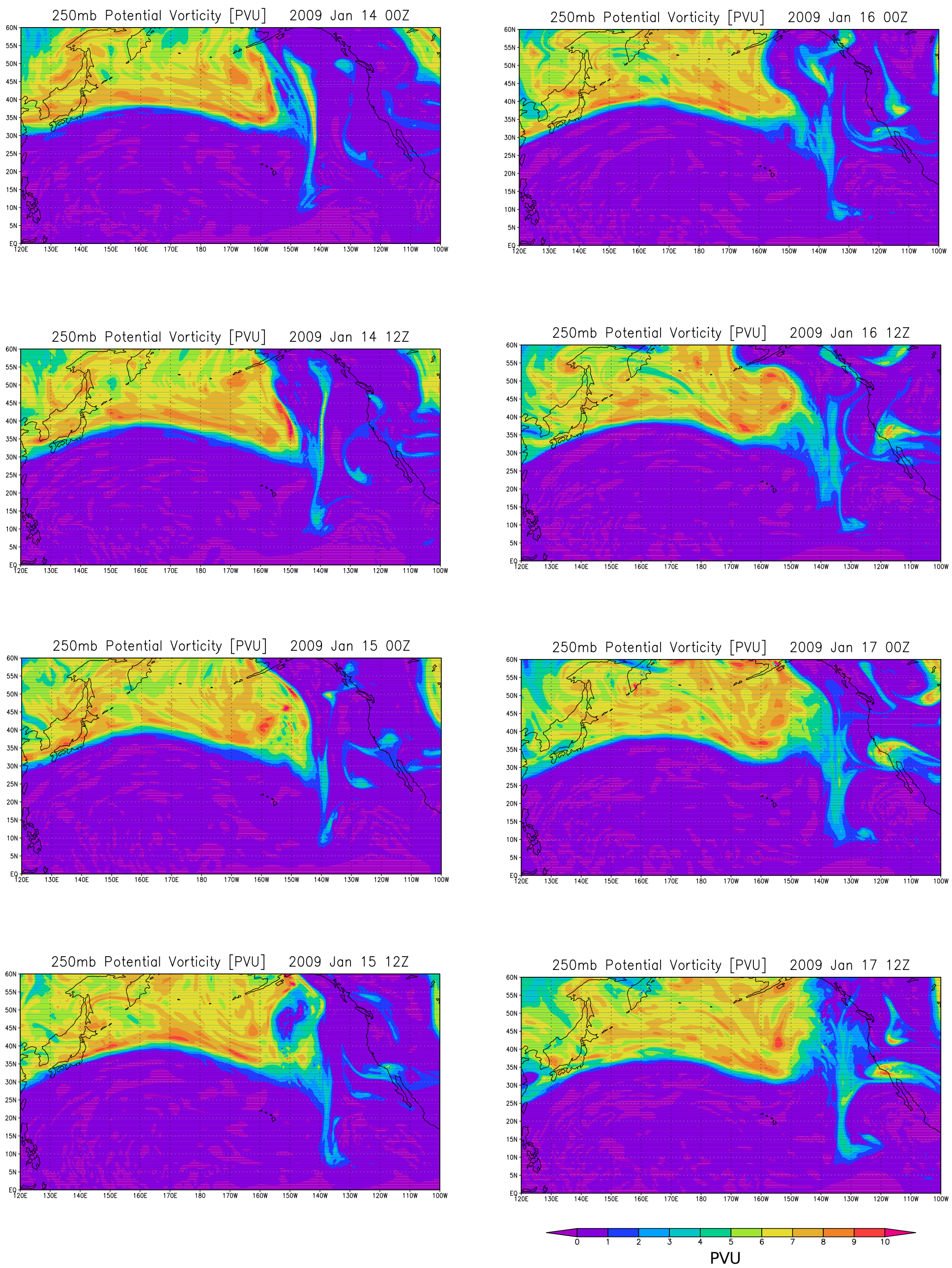

Figure 2.2: Time series of potential vorticity on the 250 hPa surface continued from Fig. 2.1. The colorbar at the bottom indicates the value of PV in PVU's.

are drawn upwards, which is seen most easily in the 300 K and 310 K isentropes.

A time near the end of the lifecycle of the intrusion is shown next. The top panel of Fig. 2.4 shows the intrusion at 00Z on 17 January 2009, which corresponds to the 7th panel

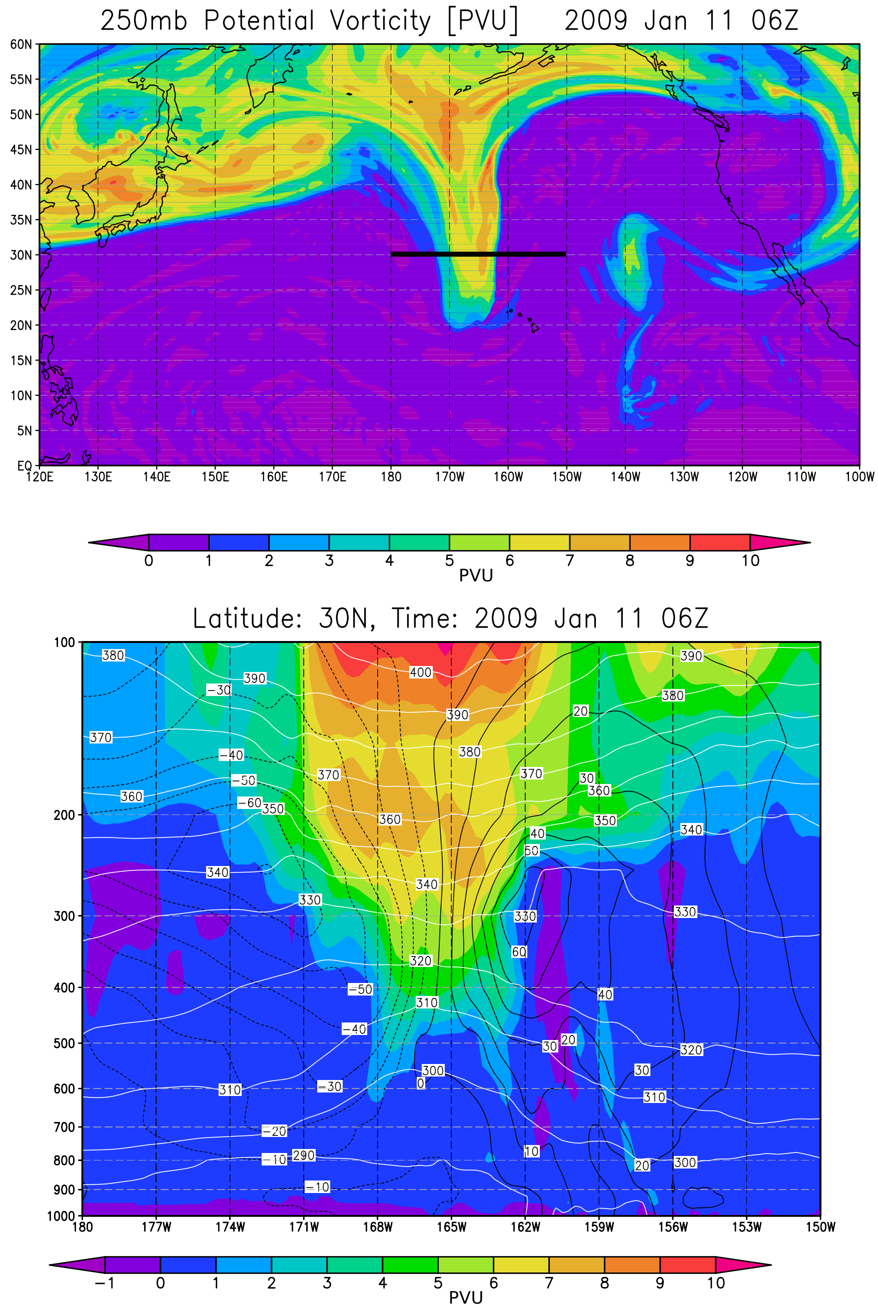

Figure 2.3: A high PV intrusion in an early stage. The top panel shows potential vorticity on the 250 hPa surface at 06Z on 11 January 2009. The thick black line indicates the location of the vertical cross-section shown in the lower panel. The lower panel shows potential vorticity (PV, colors), wind speed (v, solid and dashed black lines every 10 ms^{-1}), and potential temperature (θ, white lines every 10 K). For both panels the respective colorbar indicates PV values in PVU's.

in Fig. 2.2. At this stage the intrusion had maintained an elongated streamer appearance for several days, and then had just recently undergone a slight strengthening and widening

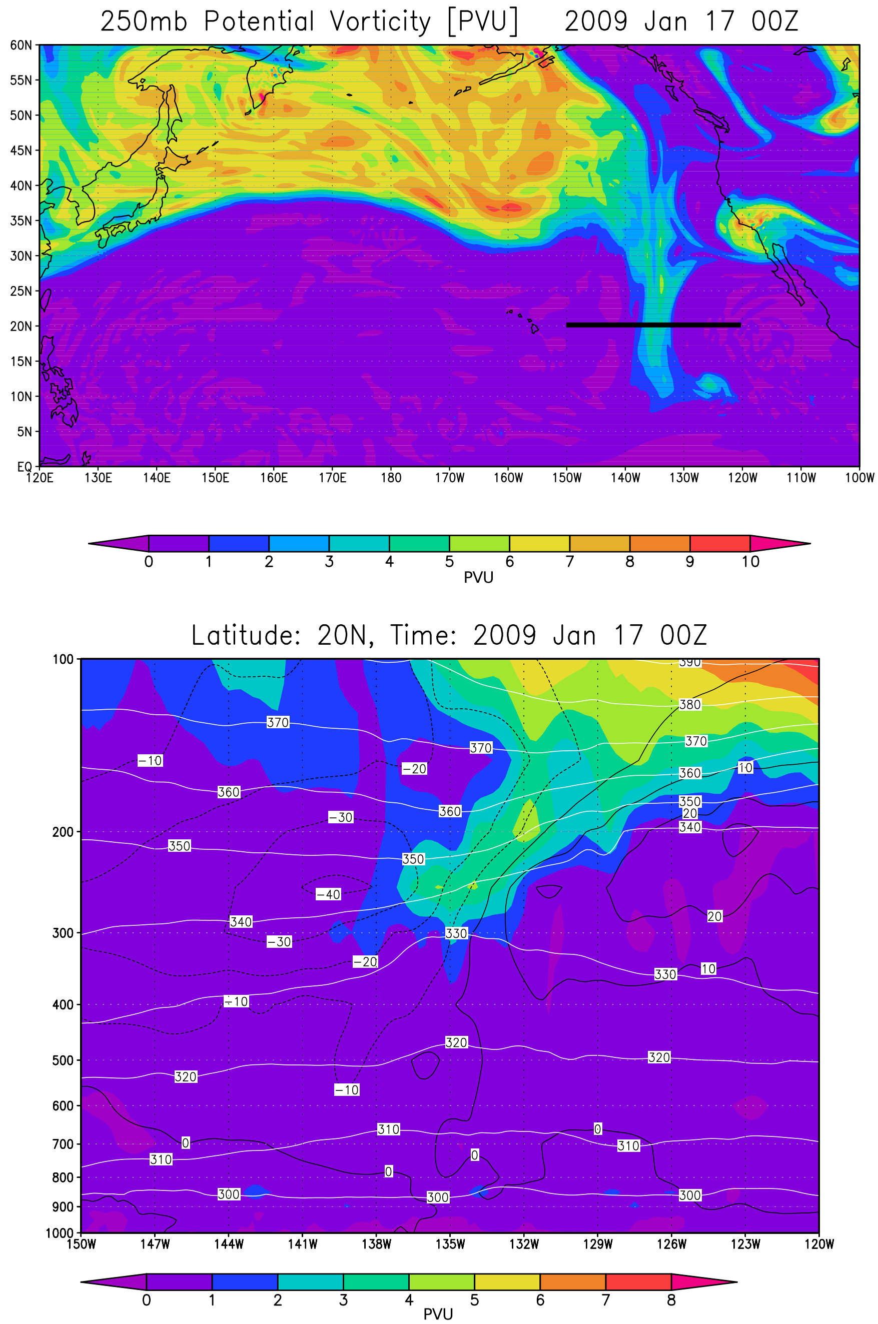

Figure 2.4: A high PV intrusion in a late stage, at 00Z on 17 January 2009. The labeling conventions are the same as in Fig. 2.3.

in the east-west direction. A cross-section is taken at 20° N and from 150° W-120° W. In the lower panel, PV, meridional winds, and isentropes are again shown. At this time the PV anomaly has retracted upwards and only reaches down to 300 hPa. The core has become somewhat more detached and reaches both downward into the troposphere and westward. The magnitude has weakened to have values just reaching 5 PVU's in the center. There are still cyclonic flow anomalies on either side of the core, though they have lost some strength. The jet on the right side maximizes at 20 m s^{-1} while on the left the southward wind reaches a minimum of -40 m s^{-1}. Directly under the PV anomaly the 330 K isentrope is seen to be drawn up towards its base.

2.2 Northward intrusion of low PV

Now we look at the case of low PV air intruding into a region of higher PV. At 00Z on 20 January 2010 a break in the meridional gradient of PV located near Japan is seen to be in the early stages of development (see the first panel of Fig. 2.5). Over the next two days, a pocket of low PV air is seen to continue to push northeastward into the PV gradient as it drifts slowly to the east. At 12Z on 22 January the low PV airmass broadens near 55° N and on 23 January the southernmost portion starts to close in with high PV air. By 24 January higher PV air has filled in around the south and the low PV air mass now exists as an entity surrounded by higher PV air. Beyond this time the low PV air mass is eroded as it undergoes mixing with the surrounding high PV air.

Our first look at the vertical structure of this low PV intrusion is taken during the early stages, and at a time when it has a lengthwise axis that is nearly north-south. At 00Z on 22 January 2010 the low PV airmass is pushing north-northeastward. The top panel of Fig. 2.6 shows the location of the cross-section marked by a thick black line; this time corresponds to the 5th panel in the lifecycle shown in Fig. 2.5. The lower panel of Fig. 2.6 shows PV, meridional winds, and isentropes, though notice the PV color scale at the bottom is colored every 3 PVU. Most of the lower and middle troposphere has values of potential vorticity just above 0 PVU. Looking at the upper troposphere we see there is a region of anomalously low PV air with some areas showing PV values just below 0 PVU

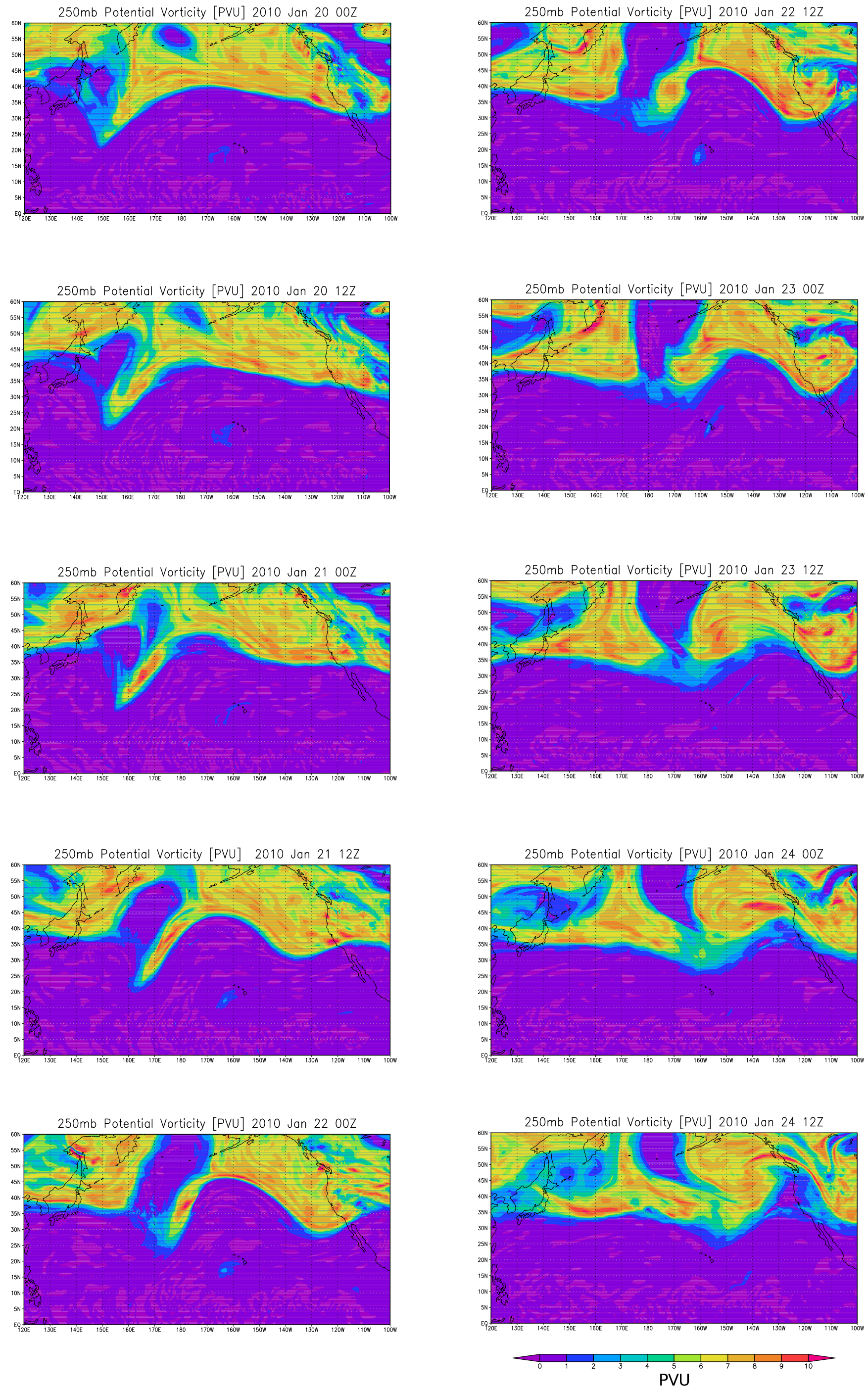

Figure 2.5: Time series of potential vorticity (PV) on the 250 hPa surface shown every 12 hours starting at 00Z on 20 January 2010. This figure shows the lifecycle of a low PV intrusion. The colorbar at the bottom indicates the values of PV in PVU's.

in the “core”, existing close to the gradient of higher PV directly overhead and having PV values above 3 PVU’s. There are anticyclonic jets on either side of the core, which appear very symmetric in shape and fairly symmetric in magnitude. The southward jet on the right side has a center that reaches a minimum of -40 m s^{-1}, and the left side has a central maximum of 60 m s^{-1}. Note that the 320 K isentrope above the core bows upward around the low PV anomaly and the 300 K isentrope located below the anomaly bows downward.

Now we look at a cross-section of the low PV intrusion at a late stage in the lifecycle, at 06Z on 24 January 2010, which corresponds to the 6 hours between the last two panels of Fig. 2.5. The top panel of Fig. 2.7 shows an airmass of low PV air completely encircled by higher PV air and having a lengthwise axis roughly north-south. The vertical cross-section is taken at 55° N from 170° E - 160° W and is shown in the lower panel of Fig. 2.7. The colorbar indicates that the PV values are colored every 2 PVU’s. The picture seen here is quite similar to that seen in Fig. 2.6, at an early stage in the lifecycle. The troposphere is composed of PV values just above 0 PVU. There is a core of low PV air, with some values just below 0 PVU, that is centered at 350 hPa and is intruding upon the gradient of high PV air directly above. There are anticyclonic flow anomalies which attain their peak values on the interface of the high and low PV air. The shape of the jets are quite symmetric about the core. On the eastern edge the minimum wind speed is -30 m s^{-1} and the western jet has a maximum of 50 m s^{-1}. The 320 K and 300 K isentropes both bow outward from the anomaly.

We have surveyed the the winter seasons during the two year period covered by the YOTC data set for potential vorticity intrusions. Events were identified by looking at the PV contours on the 250 mb surface. An event of high PV intrusion and an event of low PV intrusion were singled out for further study. Vertical cross-sections of each were plotted containing the PV, meridional wind, and potential temperature. A cross-section during the early stages of development and one during the late stages were shown for each event. A high degree of symmetry in the circulation, and the phenomenon of isentropic upglide were

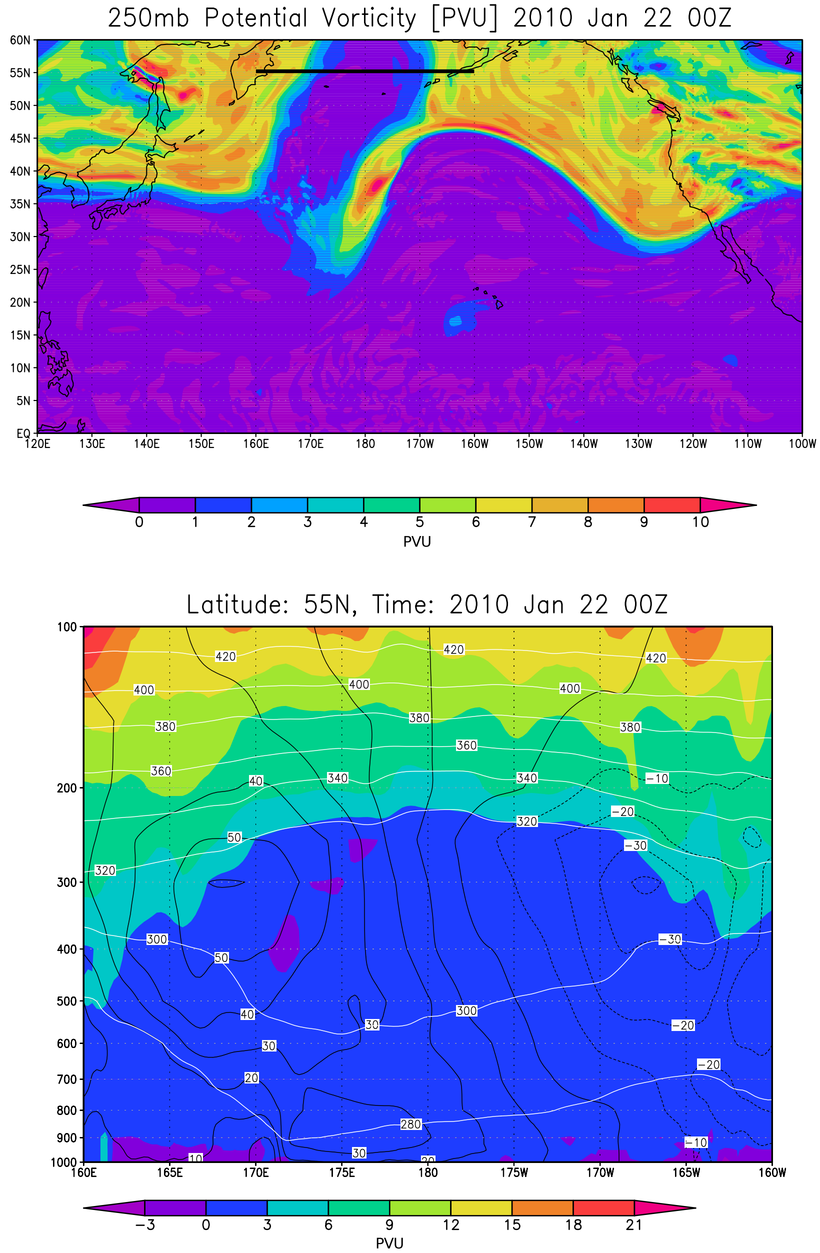

Figure 2.6: A low PV intrusion in an early stage. The top panel shows 250 hPa potential vorticity at 00Z on 22 January 2010. The thick black line indicates the location of the vertical cross-section shown in the lower panel. The lower panel shows potential vorticity (PV, colors), wind speed (v, solid and dashed black lines every 10 ms^{-1}), and potential temperature (θ, white lines every 20 K). For both panels the respective colorbar indicates PV values in PVU's.

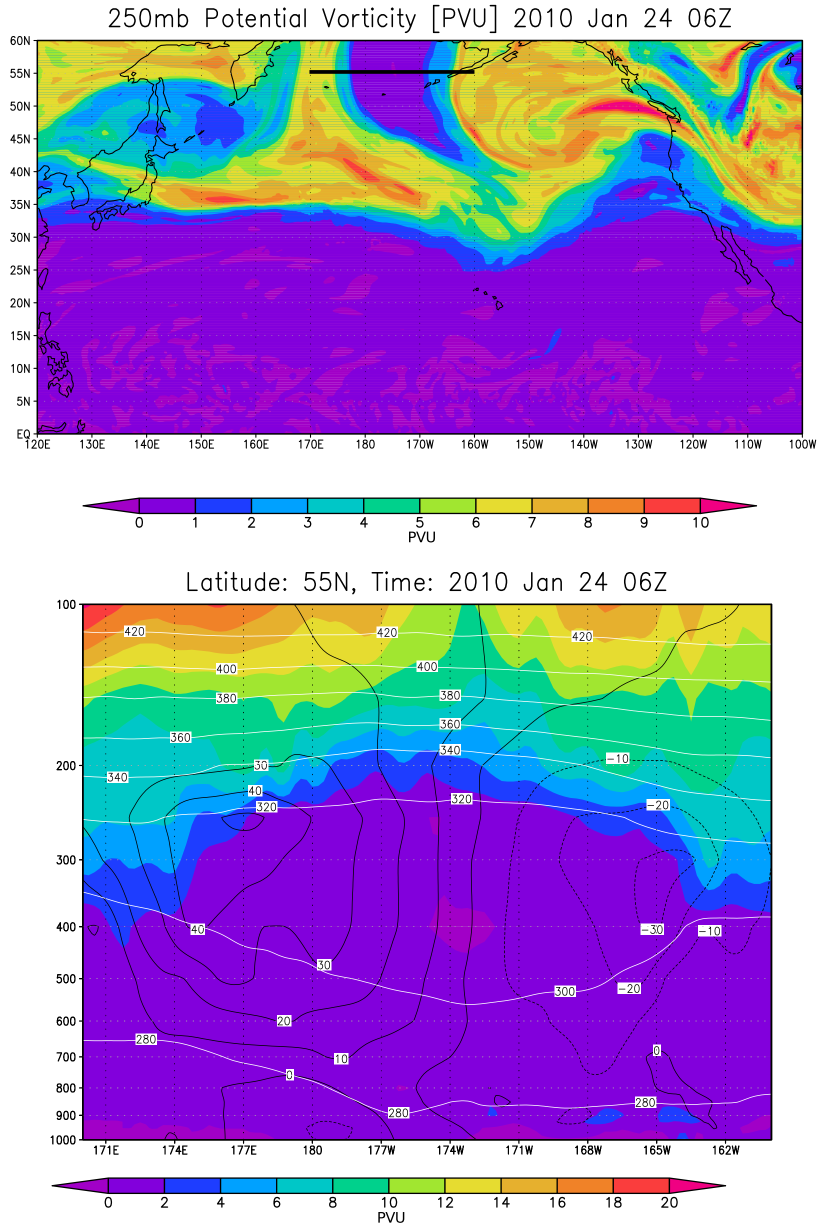

Figure 2.7: A low PV intrusion at a late stage, at 06Z on 24 January 2010. The labeling conventions are the same as in Fig. 2.6.

both present in the developing cyclonic flow. At the decaying stage, the cyclone had less symmetric circulation and weaker isentropic upglide. For the anticyclone, the circulation at each stage was quite symmetric. Both exhibited isentropes that bowed outward from the low PV anomaly.

Chapter 3

ANALYTICAL THEORY

We develop a theoretical model based on the idealization of a PV intrusion as an isolated tongue of vertically stratified air, existing in an environment with its own stratification. Neglecting any effects due to variation along the axis of the tongue, we proceed under the assumption that the intrusion is line symmetric. We then invert the potential vorticity for an ellipse shaped anomaly in the (x, θ)-plane, which is in hydrostatic balance and zonal geostrophic balance. The final results are analytical solutions.

Inspiration for this modelling problem was drawn from Gill (1981), who studied the final geostrophically adjusted flow that occurs after a finite volume of constant temperature water is intruded into a uniformly rotating, stratified ocean. This theoretical problem was motivated by the fortuitous discovery of Mediterranean eddies (or Meddies), as originally described by McDowell and Rossby (1978) and later reinterpreted by Prater and Rossby (2000). Our model differs from Gill's in that our intrusion is line symmetric and is stratified, while Gill's intrusions are homogeneous and have circular symmetry. However, like Gill, we make use of elliptical coordinates in the region outside the intrusion.

Pioneering work using potential vorticity inversion was that of Ernst Kleinschmidt (see Eliassen and Kleinschmidt Jr., 1957). Kleinschmidt modelled axisymmetric cyclones in geostrophic balance on the f-plane. The associated PV anomalies were prescribed to have an ellipse shape, and analytical solutions were found under simplifying assumptions for the background structure of the troposphere and stratosphere. These solutions differ from ours in that they are derived for the circular symmetry of a vortex. Other studies that have made use of potential vorticity inversion for anomalous PV intruding into the upper troposphere include the classic work of Hoskins et al. (1985) and Thorpe (1986). These studies looked at vorticies in gradient wind balance. Due to the nonlinearity introduced by the gradient balance assumption, the equations must be solved numerically. The solutions presented are then for disturbances having circular symmetry in gradient balance.

3.1 Primitive Equations

The starting point is the quasi-static primitive equations for invisid, adiabatic flow in physical height coordinates

$$
\begin{aligned}
\frac{Du}{Dt} - fv &= -\frac{1}{\rho}\frac{\partial p}{\partial x}, \\
\frac{Dv}{Dt} + fu &= -\frac{1}{\rho}\frac{\partial p}{\partial y}, \\
g &= -\frac{1}{\rho}\frac{\partial p}{\partial z}, \\
\frac{1}{\rho}\frac{D\rho}{Dt} + \left(\frac{\partial u}{\partial x} + \frac{\partial v}{\partial y} + \frac{\partial w}{\partial z}\right) &= 0, \\
\frac{D\theta}{Dt} &= 0.
\end{aligned}
$$

The material derivative is $D/Dt = \partial/\partial t + u\partial/\partial x + v\partial/\partial y + w\partial/\partial z$. The first law of thermodynamics is given in terms of potential temperature, $\theta = T\,(p_0/p)^{\kappa}$, where p_0 is a reference pressure and $\kappa \equiv R/c_p$ is the ratio of the gas constant for dry air and the specific heat capacity for dry air at constant pressure. Next, we convert these equations to use potential temperature (θ) as the vertical coordinate

$$
\begin{aligned}
\frac{Du}{Dt} - fv &= -\frac{\partial M}{\partial x}, \\
\frac{Dv}{Dt} + fu &= -\frac{\partial M}{\partial y}, \\
\Pi &= \frac{\partial M}{\partial \theta}, \\
\frac{1}{\sigma}\frac{D\sigma}{Dt} + \left(\frac{\partial u}{\partial x} + \frac{\partial v}{\partial y}\right) &= 0.
\end{aligned}
$$

Here the material derivative is given by

$$
\frac{D}{Dt} = \left.\frac{\partial}{\partial t}\right)_{\theta} + u\left.\frac{\partial}{\partial x}\right)_{\theta} + v\left.\frac{\partial}{\partial y}\right)_{\theta},
$$

with $\dot{\theta} = 0$ by the assumption of adiabatic flow. The continuity equation in θ-coordinates becomes a statement governing the pseudo-density, $\sigma \equiv -(1/g)(\partial p/\partial \theta)$. The Montegomery potential is $M = \theta\Pi + \Phi$, where $\Pi = c_p (p/p_0)^{\kappa}$ is the Exner function, $\Phi = gz$ the geopotential. Considering y-independent flow and writing out the material derivative terms explicitly, the governing equations are

$$
\begin{aligned}
\frac{\partial u}{\partial t} + u\frac{\partial u}{\partial x} - fv &= -\frac{\partial M}{\partial x}, \\
\frac{\partial v}{\partial t} + u\frac{\partial v}{\partial x} + fu &= 0, \\
\Pi &= \frac{\partial M}{\partial \theta}, \\
\frac{\partial \sigma}{\partial t} + u\frac{\partial \sigma}{\partial x} + \sigma\frac{\partial u}{\partial x} &= 0.
\end{aligned}
$$

Lastly, we are interested in zonally geostrophically balanced flow, so we neglect the terms related to transient motion (i.e., $\partial u/\partial t + u\partial u/\partial x$). Now, with the material derivative given by $D/Dt = \partial/\partial t + \partial/\partial x$, the governing equations become

$$fv = \frac{\partial M}{\partial x}, \tag{3.1}$$

$$\frac{Dv}{Dt} + fu = 0, \tag{3.2}$$

$$\Pi = \frac{\partial M}{\partial \theta}, \tag{3.3}$$

$$\frac{D\sigma}{Dt} + \sigma\frac{\partial u}{\partial x} = 0. \tag{3.4}$$

The domain is infinite in x, but with wind and mass field anomalies localized near the origin, so that $v \to 0$ and $p \to \tilde{p}(\theta)$ as $x \to \pm\infty$, where $\tilde{p}(\theta)$ is the specified far-field vertical profile of pressure.

3.2 Cauchy-Riemann Equations

It is straight forward to derive the potential vorticity principle from equations (3.2) and (3.4), which is a statement of material conservation

$$\frac{DP}{Dt} = 0,$$

for the potential vorticity, defined as

$$P \equiv \left(f + \frac{\partial v}{\partial x}\right)\left(-\frac{1}{g}\frac{\partial p}{\partial \theta}\right)^{-1}. \tag{3.5}$$

In the far-field the potential vorticity is

$$\tilde{P} \equiv f\left(-\frac{1}{g}\frac{\partial \tilde{p}}{\partial \theta}\right)^{-1}. \tag{3.6}$$

Because the far-field pressure ($\tilde{p}$) is only a function of θ, from (3.6) it is clear that the far-field potential vorticity is also only a function of θ, that is $\tilde{P} = \tilde{P}(\theta)$.

For converting between forms of equations it is useful to have an expression for how Π changes with p. Taking the derivative of the expression for Π with respect to p we find that $d\Pi/dp = 1/\rho\theta$. With $\tilde{\Pi} \equiv \Pi(\tilde{p})$, the analogous expression in the far-field is $d\tilde{\Pi}/d\tilde{p} = 1/\tilde{\rho}\theta$. We will use these two expressions in what follows. Now, take the ratio of (3.5) and (3.6),

$$\begin{aligned} f\frac{P}{\tilde{P}} &= \left(f + \frac{\partial v}{\partial x}\right)\left(\frac{\partial \tilde{p}/\partial \theta}{\partial p/\partial \theta}\right) \\ &= \left(f + \frac{\partial v}{\partial x}\right)\left(\frac{\tilde{\rho}(d\tilde{\Pi}/d\tilde{p})(\partial \tilde{p}/\partial \theta)}{\rho(d\Pi/dp)(\partial p/\partial \theta)}\right) \\ &\approx \left(f + \frac{\partial v}{\partial x}\right)\left(\frac{\partial \tilde{\Pi}/\partial \theta}{\partial \Pi/\partial \theta}\right), \end{aligned} \tag{3.7}$$

where the third line follows from approximating the $(\tilde{\rho}/\rho)$ factor by unity. The presence of ρ in (3.7) makes the problem weakly nonlinear. By making this approximation, which we owe to Eliassen and Kleinschmidt Jr. (1957), the problem becomes a linear one. In Section 4.4 the effect of this approximation on the solution is considered by means of a numerical model. Equation (3.7) can also be written in the form

$$\frac{\partial(v + fx)}{\partial x} + \left(\frac{\theta^2 N^2 f P}{g^2 \tilde{P}}\right)\frac{\partial \Pi}{\partial \theta} = 0, \tag{3.8}$$

where we have defined the far-field buoyancy frequency $N(\theta)$ by

$$N^2(\theta) = \frac{g^2}{\theta^2}\left(-\frac{d\tilde{\Pi}}{d\theta}\right)^{-1}. \tag{3.9}$$

For simplicity we hereafter assume that the buoyancy frequency $N(\theta)$ is inversely proportional to θ, i.e., $N(\theta) = N_c\theta_c/\theta$, where N_c and θ_c are constants. In the solution of the invertibility principle it is convenient if the two independent spatial coordinates have the same units. Thus, we define $z = [g/(\theta_c N_c f)](\theta - \theta_c)$ as the new shifted isentropic coordinate having units of length, with the constant θ_c denoting the center of the PV anomaly, and N_c the value of the buoyancy frequency at $\theta = \theta_c$. Combining (3.1) and (3.3) gives the thermal wind equation, $f(\partial v/\partial\theta) = (\partial\Pi/\partial x)$. Equation (3.8) and the thermal wind relationship can be written in the form

$$\frac{\partial(v + fx)}{\partial x} + \frac{\theta_c N_c P}{g\tilde{P}} \frac{\partial\Pi}{\partial z} = 0, \tag{3.10}$$

$$\frac{\partial(v + fx)}{\partial z} - \frac{\theta_c N_c}{g} \frac{\partial\Pi}{\partial x} = 0. \tag{3.11}$$

We conclude that the governing equations of the potential vorticity invertibility principle are the Cauchy-Riemann conditions (3.10) and (3.11), which constitute a system of first order partial differential equations for $v(x, z)$ and $\Pi(x, z)$ given $P(x, z)$. Equivalently we could obtain second order elliptic equations for v and Π by alternately eliminating the other between equations (3.10) and (3.11). The resulting equations are Laplace's equation for v and Π. We consider potential vorticity anomalies given by

$$\frac{P}{\tilde{P}} = \begin{cases} \gamma & \text{if } \; x^2/a^2 + z^2/b^2 < 1, \\ 1 & \text{if } \; x^2/a^2 + z^2/b^2 > 1, \end{cases} \tag{3.12}$$

where the constant γ specifies the magnitude of the potential vorticity within the elliptical patch whose center is at $(x, z) = (0, 0)$ and whose shape is determined by the constants a, b. To solve the invertibility problem for the potential vorticity distribution given in (3.12) we must solve (3.10) and (3.11) inside the ellipse with $P/\tilde{P}$ replaced by the constant γ, then solve (3.10) and (3.11) outside the ellipse with $P/\tilde{P}$ replaced by unity, and finally match the solutions for v and Π along the ellipse. To derive the solutions of (3.10) and (3.11) in the outer region, it is convenient to use the elliptic coordinates, (ϱ, φ). In this coordinate system ϱ plays the role of a pseudo-radius and φ the role of a pseudo-azimuth. See Appendix A for further details. In (3.12) the ellipse $x^2/a^2 + z^2/b^2 = 1$, which just encloses the region of anomalous PV, is given by $\varrho = \varrho_0 = \tanh^{-1}(b/a) = \frac{1}{2}\ln[(a+b)/(a-b)]$. Letting $P/\tilde{P} = 1$ in (3.10) and transforming (3.10) and (3.11) to elliptic coordinates results in

$$\frac{\partial(v+fx)}{\partial\varrho} + \frac{\theta_c N_c}{g}\frac{\partial\Pi}{\partial\varphi} = 0, \tag{3.13}$$

$$\frac{\partial(v+fx)}{\partial\varphi} - \frac{\theta_c N_c}{g}\frac{\partial\Pi}{\partial\varrho} = 0, \tag{3.14}$$

which are valid in the region outside the PV anomaly. The final solutions for v and Π are obtained by solving (3.10) and (3.11) inside the ellipse ($\varrho < \varrho_0$), solving (3.13) and (3.14) outside the ellipse ($\varrho > \varrho_0$), and then requiring v and Π from each region to coincide along the ellipse ($\varrho = \varrho_0$).

3.3 Solutions

As is easily confirmed by direct substitution, the solutions are

$$v(x,z) = \frac{f(\gamma-1)b/a}{\gamma+b/a}\begin{cases} x & \text{if } \varrho \le \varrho_0 \\ ae^{\varrho_0-\varrho}\cos\varphi & \text{if } \varrho \ge \varrho_0, \end{cases} \tag{3.15}$$

$$\Pi(x,z) = \tilde{\Pi}(z) + \frac{gf(\gamma-1)}{\theta_c N_c(\gamma+b/a)}\begin{cases} z & \text{if } \varrho \le \varrho_0 \\ be^{\varrho_0-\varrho}\sin\varphi & \text{if } \varrho \ge \varrho_0, \end{cases} \tag{3.16}$$

where the far-field Exner function ($\tilde{\Pi}$) is

$$\tilde{\Pi}(z) = \Pi_c - \frac{gfz}{\theta_c N_c}. \tag{3.17}$$

Since the terms in the second lines of (3.15) and (3.16) decay exponentially with ϱ, the far-field boundary conditions are satisfied. As is easily checked, the v field, given by (3.15), and the Π field, given by (3.16), are identical at $\varrho = \varrho_0$. The uniqueness of these solutions can be varified as follows. As stated above, the governing equations can be expressed in terms of Laplace's equation for v and Π in two separate domains. Boundary conditions for v and Π are specified for each domain. Since (3.15) and (3.16) both satisfy Laplace's equation as well as the boundary conditions, they are guaranteed to be the unique solutions (see Griffiths, 1999, page 116) over each domain. Now, we note that the boundary condition for the inner region can be seen as the solution from the outer region on the interface. Analogously, the solution for the inner region on the interface is the inside boundary condition for the outer region. From this observation we conclude the solutions are unique over the entire domain.

As an example, the top panel of Fig. 3.1 shows plots of (3.15) and (3.16) for $g = 9.8$ m s^{-2}, $f = 5 \times 10^{-5}$ s^{-1}, $N = 1.03 \times 10^{-2}$ s^{-1}, $\theta_c = 350$K, $\Pi_c = c_p(p_c/p_0)^\kappa$, $p_c = 200$ hPa, $a = 500$ km, $b/a = 2.30$, and $\gamma = 8$. In the construction of the top panel in Fig. 3.1, we have chosen to display isolines of v and Π (but labeled in terms of pressure) in (x, θ)-space. The bottom panel of Fig. 3.1 displays the same information, but now as isolines of v and θ in (x, p)-space. Conversion between these two representations is simply a matter of interpolation. In these plots warm colors denote positive valued isotachs (wind into the page on the right side), and the cool colors negative valued isotachs (wind out of the page on the left). This is the case of a "moderate" PV anomaly with cyclonic circulation. In the lower panel of Fig. 3.1 a characteristic of great meteorological importance is the "up-gliding" of the isentropes (black lines) beneath the PV anomaly. The 326K isentrope exhibits this upglide, and the 330K isentrope is drawn upwards to the point where it intersects the anomaly. The isentropes above the anomaly are drawn downwards. In this way the static stability is reduced both above and below the anomaly. The results shown in Fig. 3.1 are in general agreement with the observational results of Kelley and Mock (1982), and Whitfield and Lyons (1992), who have found that TUTT cells are cold core cyclones confined to the layer between 100 and 700 mb, whose typical horizontal scale is of the order of several hundred kilometers.

Modifying the parameters to $b/a = 0.198$ and $\gamma = 1/8$ gives the case of a moderate anticyclone, which is shown in Fig. 3.2. We have again displayed the solutions in both (x, θ)-space and (x, p)-space. In these figures the circulation is reversed as we would expect. Notice that in the bottom panel the isentropes directly above and below the anomaly bow

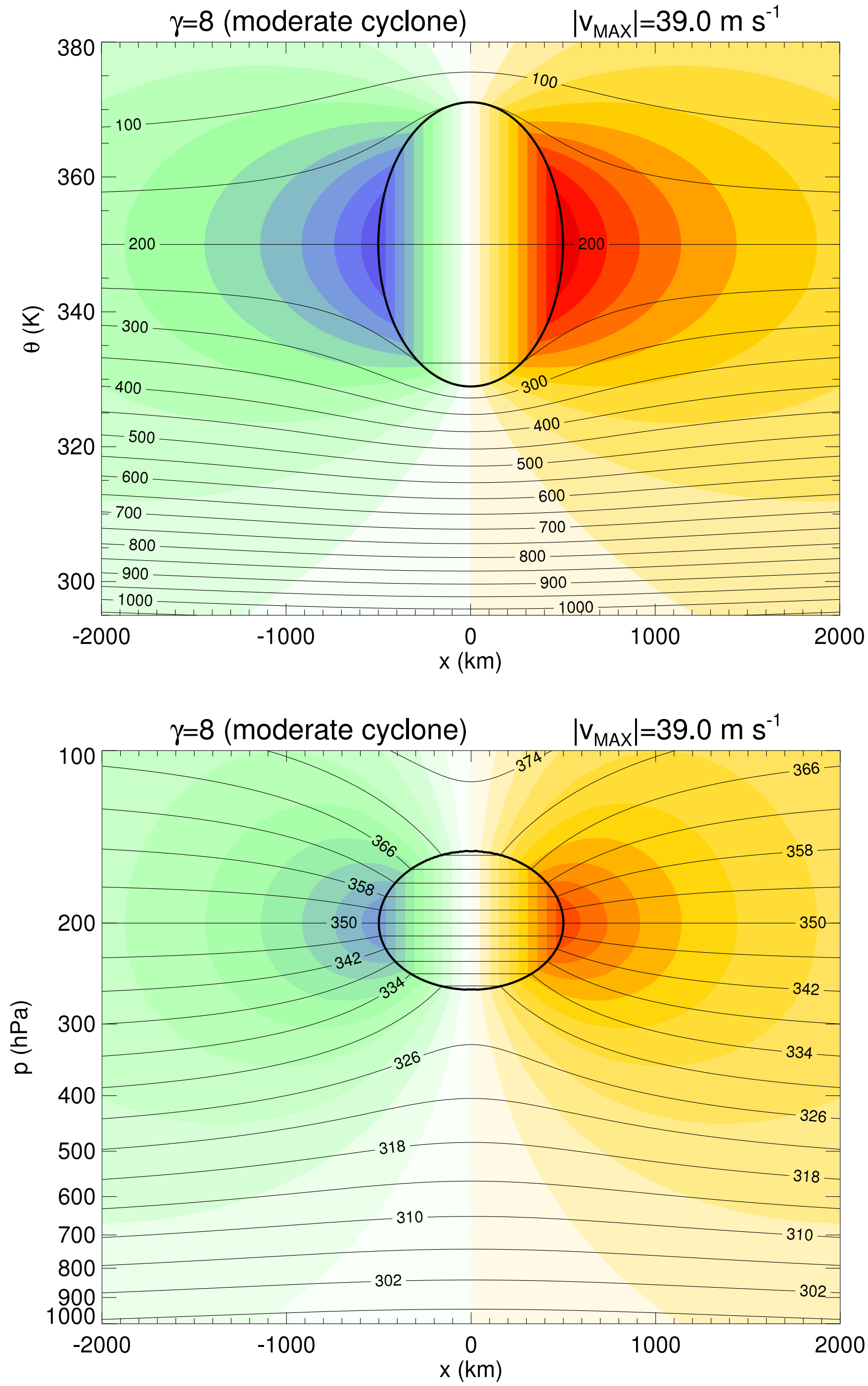

Figure 3.1: The top panel shows a cross-section of wind speed $v(x, \theta)$ and pressure $p(x, \theta)$ for cyclonic flow with the potential vorticity (PV) anomaly centered at $\theta = 350$ K and PV parameter $\gamma = 8$. Wind speed (color) is contoured every 4 m s^{-1}, and pressure (lines) is contoured every 50 hPa. The bottom panel shows the same information in the more conventional form $v(x, p)$ and $\theta(x, p)$, with the potential temperature values contoured every 4 K.

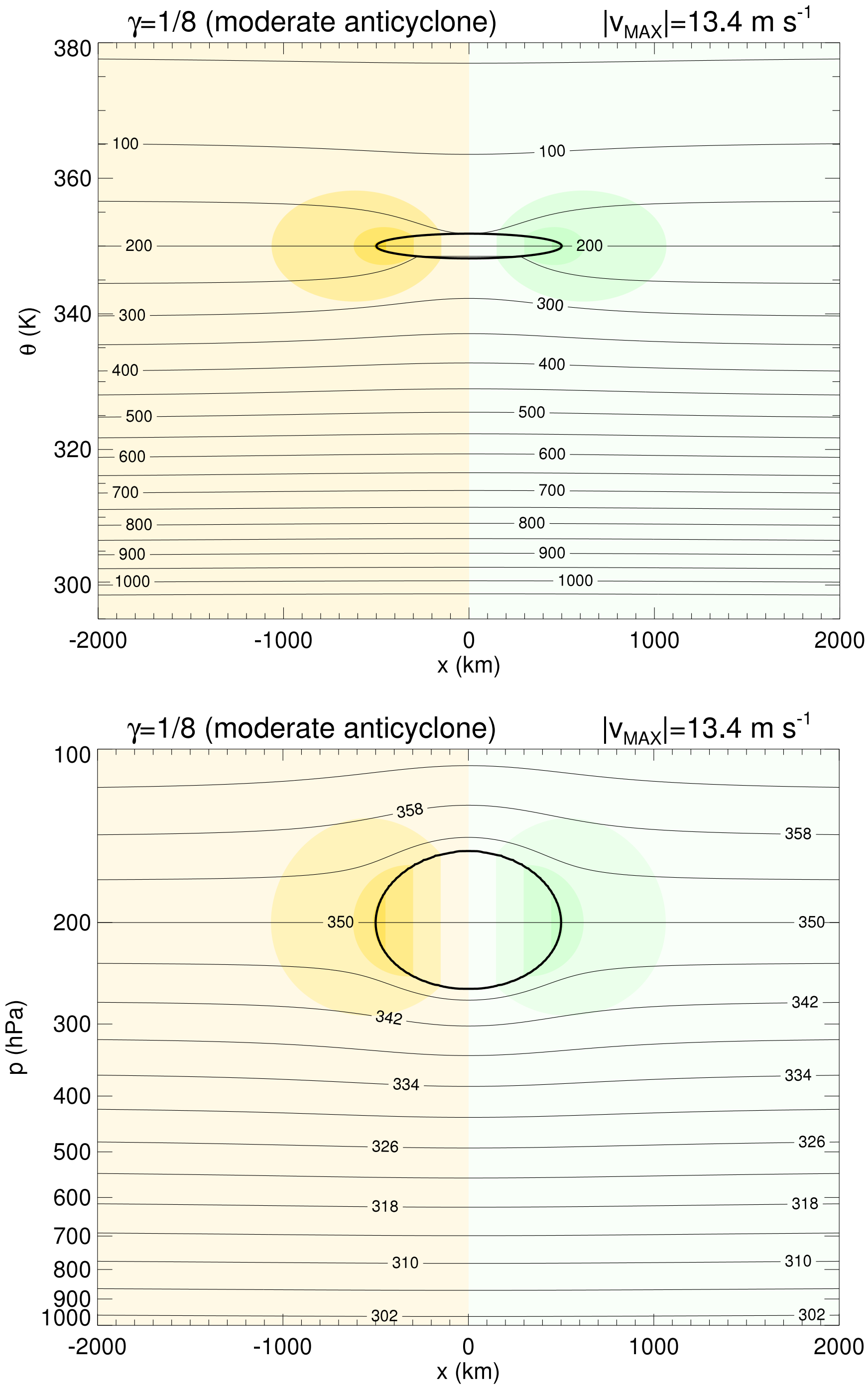

Figure 3.2: The two panels above use the same conventions as in Fig. 3.1, though for anticyclonic flow with PV parameter $\gamma = 1/8$.

outward. This effect increases the static stability in these areas. Finally, we have plotted a collection of cyclones and anticyclones that range from weak to strong in Fig. 3.6. These are shown only in the more familiar (x, p)-space. Table 3.1 contains the γ and b/a values for each case, which were determined by constraining the PV anomaly to have the same size in (x, p)-space while varying the magnitude. The thick black dashed lines will be explained in section 3.4.

An interesting feature of Fig. 1.2 is the sharp edge of the cloud field on its northwest side. This feature was investigated by Durran and Weber (1988), who used trajectory analysis to determine the cause to be preexisting moisture gradients due to air masses of different origin. A different explanation based on the solutions we have just described can be seen by referring to the moderate and strong cyclone cases shown in the left panels of Fig. 3.6. Strong upgliding motions tend to occur on isentropic surfaces that intersect the lower half of the elliptically shaped PV anomaly. The upgliding motion ends abruptly where the isentropic surfaces become horizontal inside the PV anomaly. Thus, the sharp edge of the cloud field in Fig. 1.2 can be interpreted as the west end of the isentropic upglide region and the east end of the PV anomaly.

One metric for understanding the effect of a particular PV anomaly is the maximum velocity that it induces. The maximum value of the wind speed $v_{\max}$ occurs at the two points on the left and right edges of the elliptical PV anomaly, where $x = \pm a$ and $z = 0$, or equivalently where $\varrho = \varrho_0$ and $\varphi = 0, \pi$. At these points, (3.15) yields

$$v_{\max} = fa|\gamma - 1| \left(\frac{b/a}{\gamma + b/a} \right). \tag{3.18}$$

The dimensionless coefficient in Eq. (3.18), $(|\gamma - 1| b/a) / (\gamma + b/a)$, is plotted as a function of γ and the ratio b/a in Fig. 3.3. When $\gamma = 1$ this factor is zero. Above $\gamma = 1$ corresponds to cyclonic flow, and below to anticyclonic flow. Use of this diagram alongside Eq. (3.18) allows easy estimation of the maximum wind speed. For example, with the above choices of the constants f and a, we have $fa = 25$ m s^{-1}, so that the maximum wind speed in the cyclonic flow at 200 hPa is $v_{max} = 21.3$ m s^{-1}. Now consider the case in which the center of the ellipse is placed at the surface (i.e., $\theta_c = 295$K, $\Pi_c = c_p(p_c/p_0)^\kappa$, and $p_c = p_0 = 1000$ hPa) and the PV inside the ellipse is allowed to become very large (i.e.,

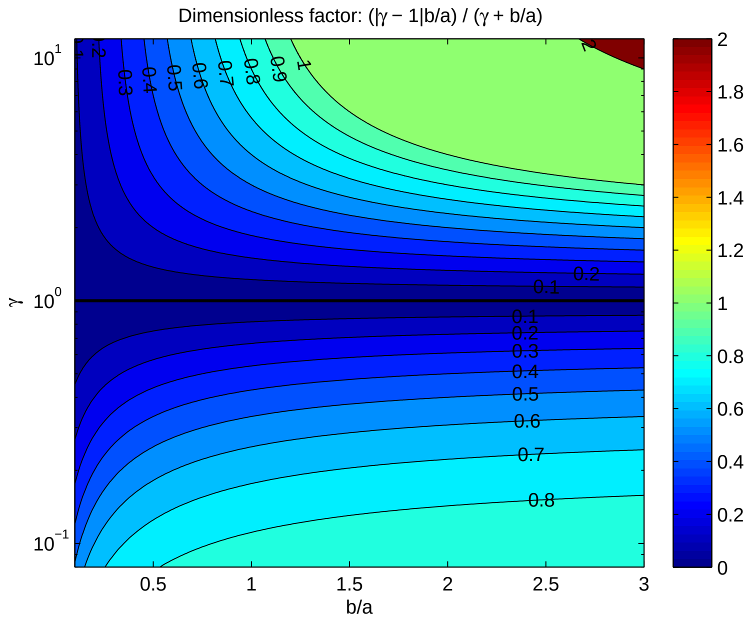

Figure 3.3: The dimensionless coefficient of Eq. (3.18) is plotted as a function of γ and b/a. The amplitude vanishes at the line $\gamma = 1$, which divides the plane into two regions: cyclonic above and anticyclonic below.

$\gamma \to \infty$). Equations (3.15) and (3.16) then reduce to

$$v(x,z) = fb \begin{cases} x/a & \text{if } \varrho \le \varrho_0 \\ e^{\varrho_0 - \varrho}\cos\varphi & \text{if } \varrho \ge \varrho_0, \end{cases} \tag{3.19}$$

$$\Pi(x,z) = \Pi_c - \frac{gfb}{\theta_c N_c} \begin{cases} 0 & \text{if } \varrho \le \varrho_0 \\ z/b - e^{\varrho_0 - \varrho}\sin\varphi & \text{if } \varrho \ge \varrho_0. \end{cases} \tag{3.20}$$

Note from (3.20) that Π, and hence p, are constant in the ellipse (the massless layer).

The top panel of Fig. 3.4 shows isolines of $v(x,\theta)$ and $p(x,\theta)$, computed from (3.19) and (3.20) for the parameters $g = 9.8$ m s^{-2}, $f = 5 \times 10^{-5}$ s^{-1}, $N_c = 1.03 \times 10^{-2}$ s^{-1}, $a = 500$ km, and $b = 634$ km. The bottom panel displays the same information, but in the more conventional form $v(x,p)$ and $\theta(x,p)$. Note that the half-ellipse region in the top panel is the massless layer and that it becomes infinitesimally thin in the bottom panel. For the chosen parameters, the peak wind anomaly is 31.7 m s^{-1} and the surface potential

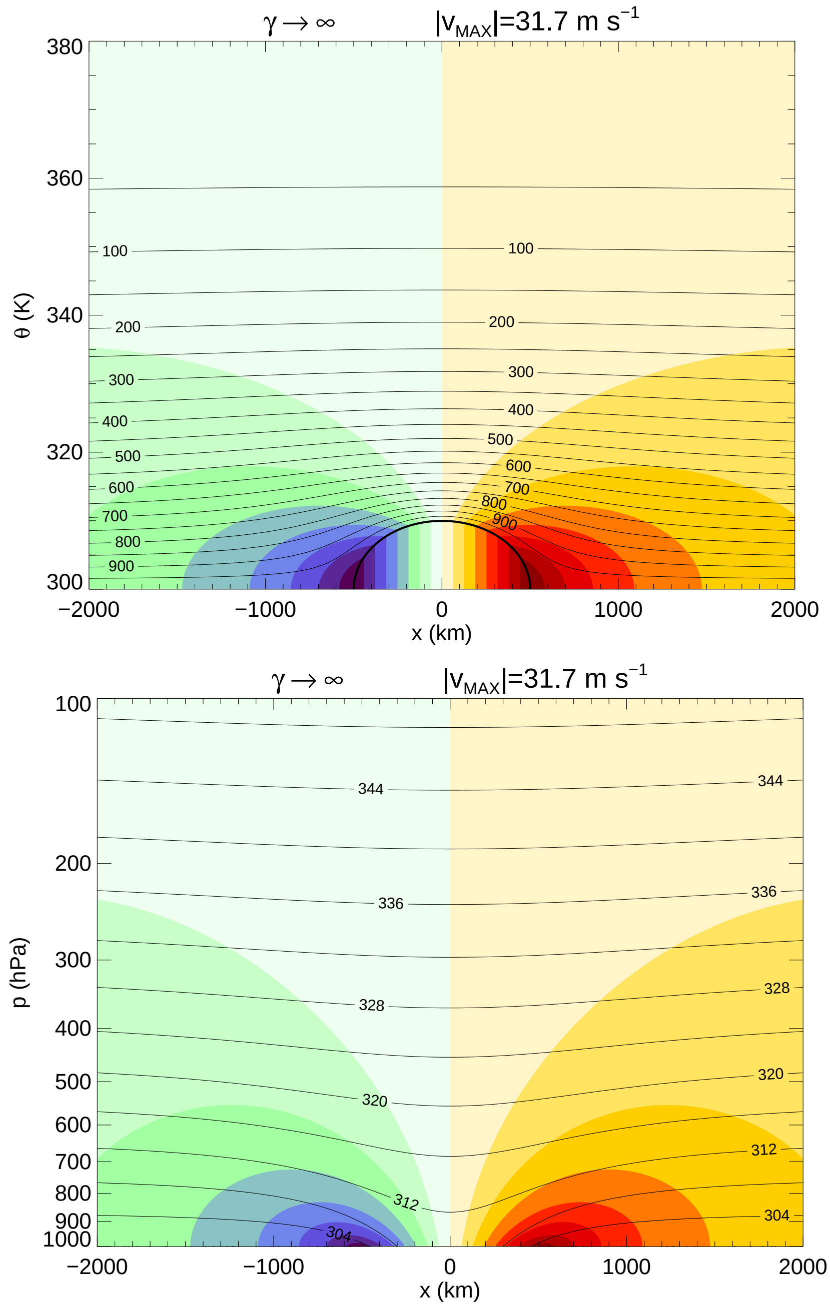

Figure 3.4: The two panels above show cross-sections of a cyclonic flow anomaly located at the surface with PV parameter $\gamma \to \infty$. The labeling conventions are the same as in Fig. 3.1.

temperature anomaly is 10 K, which allows for a rough comparison of the present analytical results with the numerical results shown in Fig. 16a of Hoskins et al. (1985) and in Fig. 4 of Thorpe (1986). In making such a rough comparison, it should be kept in mind that the present analytical results are for line symmetry and geostrophic balance, while the numerical results are for circular symmetry and gradient balance.

3.4 Partitioning of the PV

The solutions (3.15) and (3.16) are useful for understanding how the PV is partitioned between vorticity and static stability. For example, by differentiation of (3.15) and (3.16) it can be shown that the dimensionless isentropic absolute vorticity is given by

$$\frac{f + (\partial v/\partial x)}{f} = \frac{1}{\gamma + b/a} \begin{cases} \gamma(1 + b/a) & \text{if } \varrho < \varrho_0 \\ \gamma + b/a + (\gamma - 1)F & \text{if } \varrho > \varrho_0, \end{cases} \tag{3.21}$$

and the dimensionless (inverse) static stability by

$$\frac{(\partial\Pi/\partial\theta)}{(\partial\tilde{\Pi}/\partial\theta)} = \frac{1}{\gamma + b/a} \begin{cases} 1 + b/a & \text{if } \varrho < \varrho_0 \\ \gamma + b/a + (\gamma - 1)F & \text{if } \varrho > \varrho_0, \end{cases} \tag{3.22}$$

where

$$F(\varrho, \varphi) = e^{\varrho_0 - \varrho} \begin{cases} \dfrac{b}{c}\left(\dfrac{\cosh\varrho\sin^2\varphi - \sinh\varrho\cos^2\varphi}{\cosh^2\varrho\sin^2\varphi + \sinh^2\varrho\cos^2\varphi}\right) & \text{if } a > b \\ \dfrac{b}{c}\left(\dfrac{\sinh\varrho\sin^2\varphi - \cosh\varrho\cos^2\varphi}{\sinh^2\varrho\sin^2\varphi + \cosh^2\varrho\cos^2\varphi}\right) & \text{if } a < b. \end{cases} \tag{3.23}$$

Note that (3.21) divided by (3.22) yields

$$\left(\frac{f + (\partial v/\partial x)}{f}\right)\left(\frac{\partial\tilde{\Pi}/\partial\theta}{\partial\Pi/\partial\theta}\right) = \begin{cases} \gamma & \text{if } \varrho < \varrho_0 \\ 1 & \text{if } \varrho > \varrho_0, \end{cases} \tag{3.24}$$

which is the normalized version of (3.7). Within the ellipse, the partitioning of the dimensionless PV between the absolute vorticity and the static stability is

$$\left(\frac{\gamma(1 + b/a)}{\gamma + b/a}\right)\left(\frac{\gamma + b/a}{1 + b/a}\right) = \gamma,$$

so that the partitioning depends only on γ and b/a. In this sense, all vortices with the same γ and the same b/a are dynamically similar. For the example shown in Fig. 3.1, $\gamma = 8$ and $b/a = 2.30$, so that the partitioning is $(2.56)(3.12) = (2.83)^2 = 8$, i.e., the PV inversion in

γ	b/a	$v_{\max}$ (m s^{-1})	$\left(\frac{f+(\partial v/\partial x)}{f}\right)\left(\frac{\partial\tilde{\Pi}/\partial\theta}{\partial\Pi/\partial\theta}\right)=\gamma$	$\alpha(\gamma, b/a)$
12	2.84	52.6	$(3.11)(3.86) = (3.46)^2 = 12$	0.804
8	2.30	39.0	$(2.56)(3.12) = (2.83)^2 = 8$	0.820
4	1.59	21.3	$(1.85)(2.16) = (2.00)^2 = 4$	0.858
1/4	0.316	10.5	$(.581)(.430) = (.500)^2 = 1/4$	1.35
1/8	0.198	13.4	$(.463)(.270) = (.354)^2 = 1/8$	1.72
1/12	0.148	14.7	$(.413)(.202) = (.289)^2 = 1/12$	2.05

Table 3.1: Ratio of the dimensionless isentropic absolute vorticity (3.21) to the dimensionless static stability (3.22) for select values of dimensionless potential vorticity magnitude (γ) and shape (b/a). Cyclonic vortices, where $\gamma > 1$, range from strongest ($\gamma = 12$) to weakest ($\gamma = 4$), and anticyclonic vortices, where $\gamma < 1$, range from weakest ($\gamma = 1/4$) to strongest ($\gamma = 1/12$).

this case is biased toward stability, with a dimensionless absolute vorticity of 2.56 and a dimensionless stability of 3.12.

Another way to quantify the partitioning within the ellipse is through the ratio

$$\alpha(\gamma, b/a) = \frac{(f + \partial v/\partial x)/f}{(\partial\tilde{\Pi}/\partial\theta)/(\partial\Pi/\partial\theta)} = \frac{\gamma(1 + b/a)^2}{(\gamma + b/a)^2}, \tag{3.25}$$

which is the product of the dimensionless absolute vorticity and the dimensionless (inverse) static stability. Figure 3.5 shows isolines of $\alpha(\gamma, b/a)$ as a function of γ and b/a. Cases with $\alpha > 1$ are vorticity biased, while cases with $\alpha < 1$ are stability biased. For the example shown in Fig. 3.1, $\alpha = 0.820$, so the anomaly is stability biased as previously shown.

We now discuss the partioning in the region outside of the PV anomaly. Like PV itself, both $(\partial v/\partial x)$ and $(\partial\Pi/\partial\theta)$ are in general discontinuous across the ellipse. However, four locations on the ellipse are special. At $(x, z) = (0, -b)$ and $(x, z) = (0, b)$, we find that $F = b/a$, so that the vorticity is continuous but the stability experiences its largest jump. Similarly, at $(x, z) = (-a, 0)$ and $(x, z) = (a, 0)$, we find that $F = -1$, so that the stability is continuous but the vorticity experiences its largest jump. The dashed lines in Fig. 3.6 are lines along which $F = 0$, so that $(\partial v/\partial x) = 0$ and $(\partial\Pi/\partial\theta) = (\partial\tilde{\Pi}/\partial\theta)$. These four dashed lines divide the region outside the ellipse into four subregions. Above and below the ellipse, two subregions of enhanced vorticity and reduced stability fan out vertically, while to the left and right of the ellipse, two subregions of reduced vorticity and

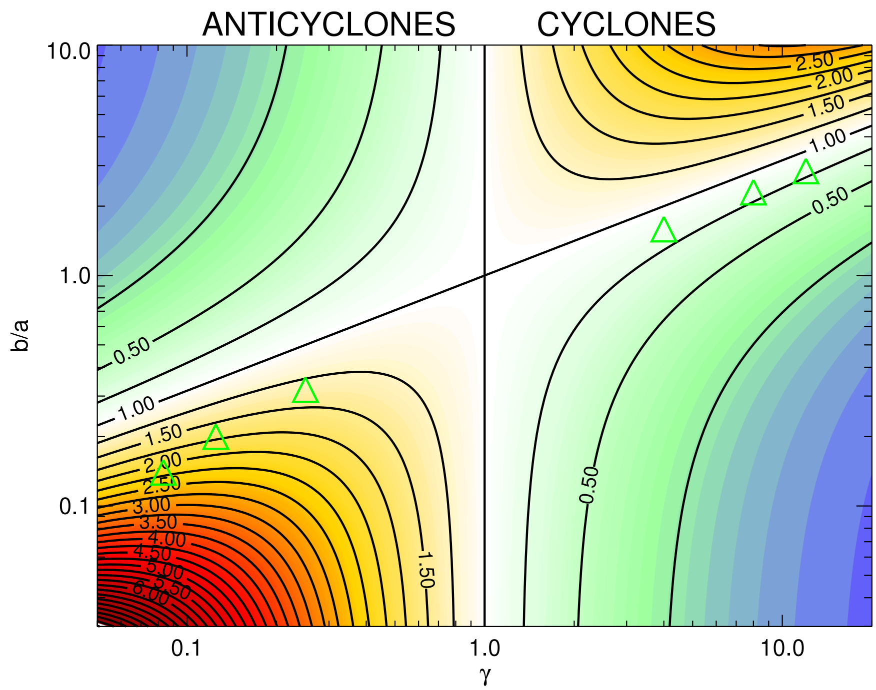

Figure 3.5: Isolines of $\alpha(\gamma, b/a)$, as defined in (3.25). PV inversion is vorticity-biased for cases in which $\alpha > 1$ (red/orange) and stability-biased for cases in which $\alpha < 1$ (blue/green). The six triangles correspond to the six cases detailed in Table 3.1 and shown in Fig. 3.6.

enhanced stability fan out horizontally. It should be noted that Wirth (2000) partitioned PV into thermal (static stability) and dynamical (vorticity) components via the quasi-geostrophic perturbation potential vorticity and the use of Fourier modes. Expressions for the components were given in terms of the perturbation PV and a coefficient that depended only on the aspect ratio of the Fourier modes. The partioning given by (3.21) and (3.22) are more versatile than the quasi-geostrophic partioning of Wirth because they allow for large relative vorticities compared with f. An additional difference is that our partitioning is expressed in terms of a localized PV anomaly specified in our chosen coordinates. We have derived a theoretical model based on a simplified view of a potential vorticity intrusion having line symmetry. Simple analytical solutions were found describing the flow inside and outside of the ellipse shaped anomaly. The solution for the meridional wind led to an equation for the maximum wind speed induced by the anomaly. Lastly, we used the solutions to partition the potential vorticity into it's vorticity and static stability components.

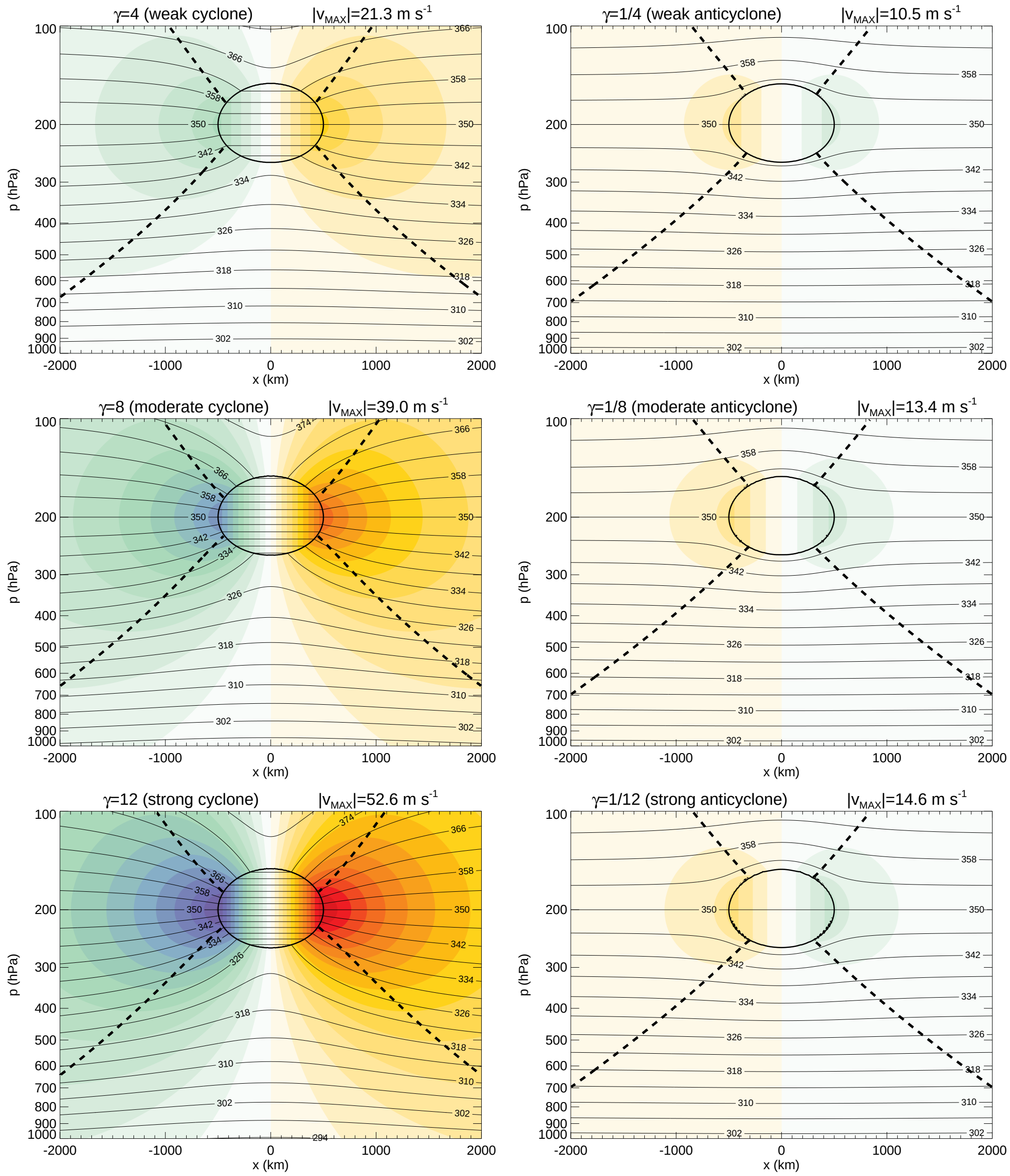

Figure 3.6: Cross-section plots of wind speed (v, colors) and potential temperature (θ, lines) for PV anomalies with select values of the parameter γ. Cyclones of increasing intensity are shown in the left column (γ=4,8,12), and anticyclones of increasing intensity are shown in the right column (γ=1/4,1/8,1/12). Wind speed values are contoured every 4 m s^{-1}, and potential temperature values are contoured every 4 K. The region of enhanced PV is outlined by the thick black ellipse, whose shape is defined by a=500 km and by the six different values of b/a given in Table 3.1.

Chapter 4

NUMERICAL STUDY

The numerical modelling study solves the unapproximated equations of Chapter 3 by numerical integration. Two aspects we are then able to address are: (1) the lack of a stratosphere, (2) the approximation of the density by the far-field density.

In the first section the model equations are described. Then we take a small detour to establish values for a parameter that we must prescribe, the buoyancy frequency. Next we look at the general solutions. Finally, we look at the two approximations listed above.

4.1 Model Description

The most convenient form of the model for computation is expressed in terms of the Montgomery potential, M. The starting point is the definition of the potential vorticity (P),

$$P \equiv \left(f + \frac{\partial v}{\partial x}\right)\left(-\frac{1}{g}\frac{\partial p}{\partial \theta}\right)^{-1}. \tag{4.1}$$

Making use of the expression $d\Pi/dp = 1/\rho\theta$ in (4.1) we get

$$\frac{f\theta\rho P}{g}\frac{\partial \Pi}{\partial \theta} + \frac{\partial\,(fv)}{\partial x} = -f^2.$$

Now applying the statement of hydrostatic balance $\Pi = \partial M/\partial\theta$ as well as that of zonal geostrophic balance, $fv = \partial M/\partial x$, we arrive at a second order elliptic equation for the Montgomery potential,

$$\frac{g}{f\theta\rho P}\left(f^2 + \frac{\partial^2 M}{\partial x^2}\right) + \frac{\partial^2 M}{\partial \theta^2} = 0.$$

This equation is discretized by finite difference and solved on the interior of the domain by successive overrelaxation (SOR). On the lateral boundaries the Montgomery potential is held at the prescribed far-field value, $\tilde{M}(\theta)$. At the lower boundary the relationship $M = \theta\,(\partial M/\partial\theta) + \phi$ is used, where we have let $\phi = 0$ for no topography. The top boundary condition is given by the hydrostatic relationship applied on a constant pressure surface. The complete specification of the problem is as follows:

$$\frac{g}{f\theta\rho P}\left(f^2 + \frac{\partial^2 M}{\partial x^2}\right) + \frac{\partial^2 M}{\partial \theta^2} = 0 \quad \text{in the interior,} \tag{4.2}$$

$$\rho = \frac{p_0}{R\theta}\left(\frac{1}{c_p}\frac{\partial M}{\partial \theta}\right)^{(1-\kappa)/\kappa}, \tag{4.3}$$

$$M = \tilde{M}(\theta) \quad \text{at } x = \pm L, \tag{4.4}$$

$$\frac{\partial M}{\partial \theta} = \Pi_T \quad \text{at } \theta = \theta_T, \tag{4.5}$$

$$M - \theta\frac{\partial M}{\partial \theta} = 0 \quad \text{at } \theta = \theta_B. \tag{4.6}$$

The details of the discretization and the SOR procedure are given in Appendix B.

4.2 Buoyancy frequency

The buoyancy frequency, which is a measure of static stability in the atmosphere, is a defined quantity in our theory that must be specified. From Gill (1982, page 54), buoyancy frequency is defined as

$$N^2 = \frac{g}{\theta}\frac{d\theta}{dz}. \tag{4.7}$$

For guidance we look at observations of the vertical profile of the atmosphere. The data used is taken from Fulton and Schubert (1985) and consists of mean temperature given at pressure levels for two locations in the tropics, the Marshall Islands and GATE. The Marshall Islands are located just west of the international date line, around 10°-15° N, and GATE (Global Atmospheric Research Program, GARP Atlantic Tropical Experiment) took place just south of the Cape Verde Islands, near 10° N. Tropical locations were chosen because our primary interest is intrusions of high PV into low latitudes.

To calculate buoyancy frequency from the two soundings we express equation (4.7) in terms of temperature and pressure,

$$N^2 = -\frac{g}{T}\left[\frac{gp}{TR}\frac{dT}{dp} - \frac{g}{c_p}\right]. \tag{4.8}$$

Letting $T \rightarrow \bar{T}$, and then approximating the derivative term as a finite difference, the resulting buoyancy frequency profiles are shown in Fig. 4.1. The main features to observe

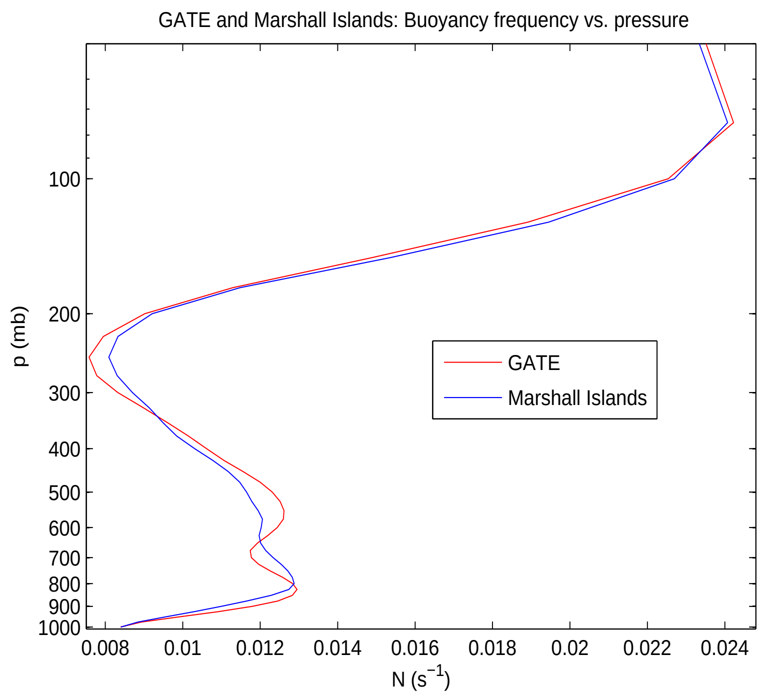

Figure 4.1: Buoyancy frequency (s^{-1}) is calculated from Eq. (4.8) using sounding data from two locations in the tropics.

are the general decrease with height in the troposphere, followed by a sharp increase at the tropopause, and then a slight decrease with height in the stratosphere. In the analytical theory we modelled the trend of N decreasing with height in the troposphere by defining it to be inversely proportional to potential temperature. We will use this same definition for the troposphere only solutions in the next section. In Section 4.5 we modify this definition to include a stratosphere by making N a piecewise function of potential temperature.

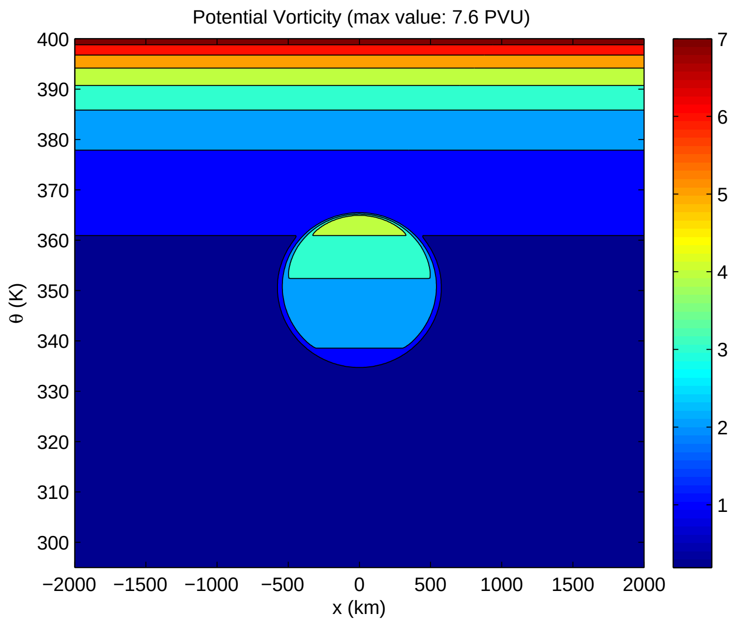

Figure 4.2: The prescribed potential vorticity field, $P(x, \theta)$, for the case of a weak cyclone having $\gamma = 4$ and ratio $b/a = 1.59$. The colorbar indicates the filled contour values in PVU's.

4.3 Solutions

In the analytical model the prescribed PV contains a discontinuous jump by the factor γ at the edge of the ellipse-shaped anomaly. In the numerical relaxation we modify the definition from (3.12) to (4.9) so that it contains a smooth transition between the anomaly and the background field. In (4.9) the variable ϱ is the pseudo-radius of the elliptical coordinate system (see appendix A), and the function S is defined by $S(s) = 1 - 3s^2 + 2s^3$. To understand the role of $S(s)$ note that $S(0) = 1$ and $S(1) = 0$. Looking at the middle line of (4.9), when $\varrho = \varrho_1$ the expression evaluates to γ. When $\varrho = \varrho_2$ the same expression evaluates to 1. The derivative at these points are $S'(0) = 0$ and $S'(1) = 0$. From these considerations it is clear that between ϱ_1 and ϱ_2 the PV anomaly continuously takes on values between γ and 1, and is smooth at these points as well. In the limit $\varrho_1 \to \varrho_2$, definition (4.9) approaches definition (3.12). The potential vorticity field when $\gamma = 4$, $a = 500$ km, and $b/a = 1.59$ is shown in Fig. 4.2. The background PV field increases with potential temperature in the vertical. Inside the anomaly the PV increases upwards as well, but is also multiplied by the factor γ.

$$\frac{P}{\tilde{P}} = \begin{cases} \gamma & \text{if } \ 0 \le \varrho \le \varrho_1, \\ \gamma S\left(\frac{\varrho-\varrho_1}{\varrho_2-\varrho_1}\right) + S\left(\frac{\varrho_2-\varrho}{\varrho_2-\varrho_1}\right) & \text{if } \ \varrho_1 \le \varrho \le \varrho_2, \\ 1 & \text{if } \ \varrho_2 \le \varrho \le \infty, \end{cases} \tag{4.9}$$

Figure 4.3 displays solutions to the problem stated in Eqs. (4.2)—(4.6). These solutions are not directly comparable to those presented in Fig. 3.6 for several reasons. First the boundary conditions are different. While the effect of the localized PV forcing decays with distance in the analytical model, the numerical model obeys the conditions (4.4)—(4.6). Second, the density is approximated by the far-field density in the analytical model. In the numerical model we can work with the unapproximated density, or the far-field density, which we take up in the next section. Lastly, by introducing the smoothed PV anomaly (4.9) where ρ_0 and ρ_1 coincide, the anomaly is effectively larger in the numerical case than in the analytical case. This is reflected in the larger maximum wind speeds that are seen in Fig. 4.3. The idea then is to compare the base numerical solutions with the density approximated numerical solutions in Section 4.4, and with the stratosphere added numerical solutions in Section 4.5. This will provide use with a sense of the effect of each approximation made in the analytical case, based on what we learned from comparison of the different numerical cases.

One thing to note is that the shape of the PV anomaly in pressure space is not constant in the numerical solutions like it is in the analytical solutions. This may be expected because the relationship derived for the shape was based on the linearized equations, so this relationship is not, in general, valid for the nonlinear numerical equations.

4.4 Density approximation

In the analytical theory (see Eq. (3.7)) the ratio of the density with the far-field density is approximated by unity, or $\tilde{\rho}/\rho \to 1$. In the formulation of the numerical model the

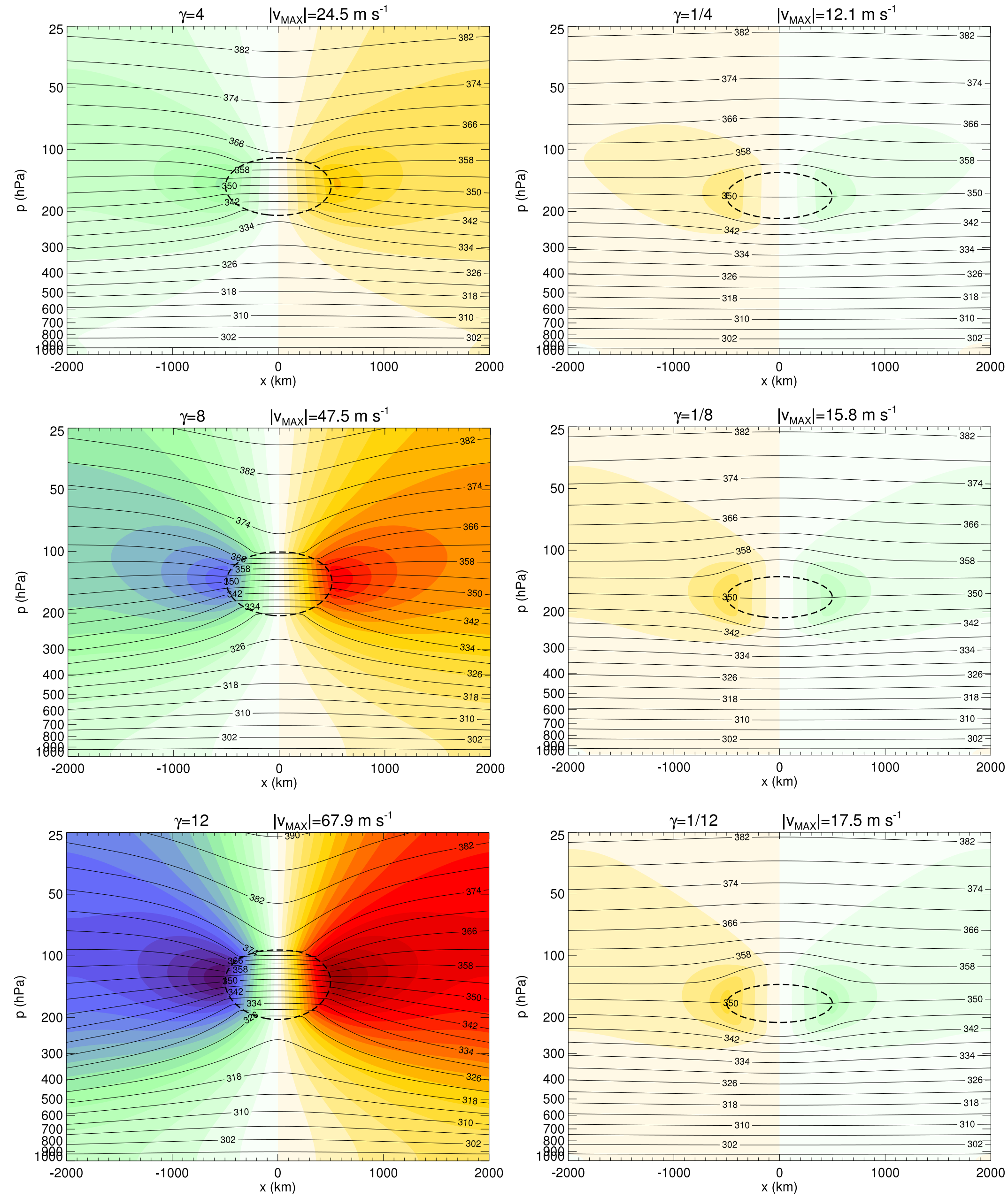

Figure 4.3: Cross-section plots of wind speed (v, colors) and potential temperature (θ, lines) for PV anomalies with select values of the parameter γ. Cyclones of increasing intensity are shown in the left column (γ=4,8,12), and anticyclones of increasing intensity are shown in the right column (γ=1/4,1/8,1/12). Wind speed values are contoured every 4 m s^{-1}, and potential temperature values are contoured every 4 K. The region of enhanced PV (see top line in (4.9)) is outlined by the dashed black ellipse, whose shape is defined by a=500 km and by the six different values of b/a given in Table 3.1.

density alone is present, see Eq. (4.2). The analogous approximation then is to hold the density at its far-field value, or $\rho \rightarrow \tilde{\rho}$. The numerical solutions for this density approxi-

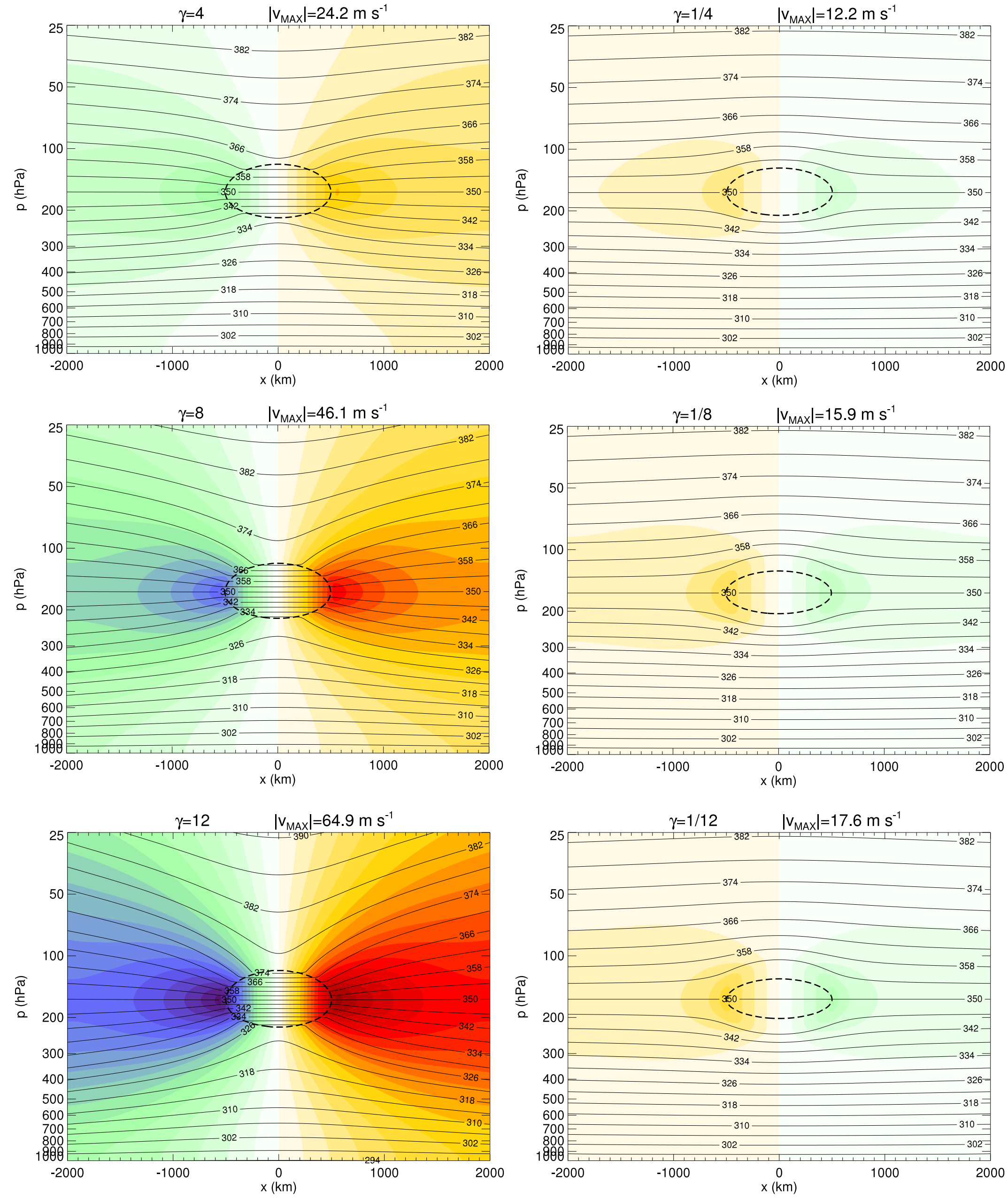

Figure 4.4: The conventions are the same as in Fig. 4.3, though the density, ρ, is held at the far-field value, $\tilde{\rho}$.

mation are displayed in Fig. 4.4. Comparing with Fig. 4.3 we see that the maximum wind speeds vary between the two but not by alot. For the cyclones, the density approximated solutions are slower, with this effect increasing as the intensity increases. The difference between the cyclones for $\gamma = 12$ is 3 m s^{-1}. For the anticyclones the density approximated solutions are faster. The difference in all three cases is just 0.1 m s^{-1}.

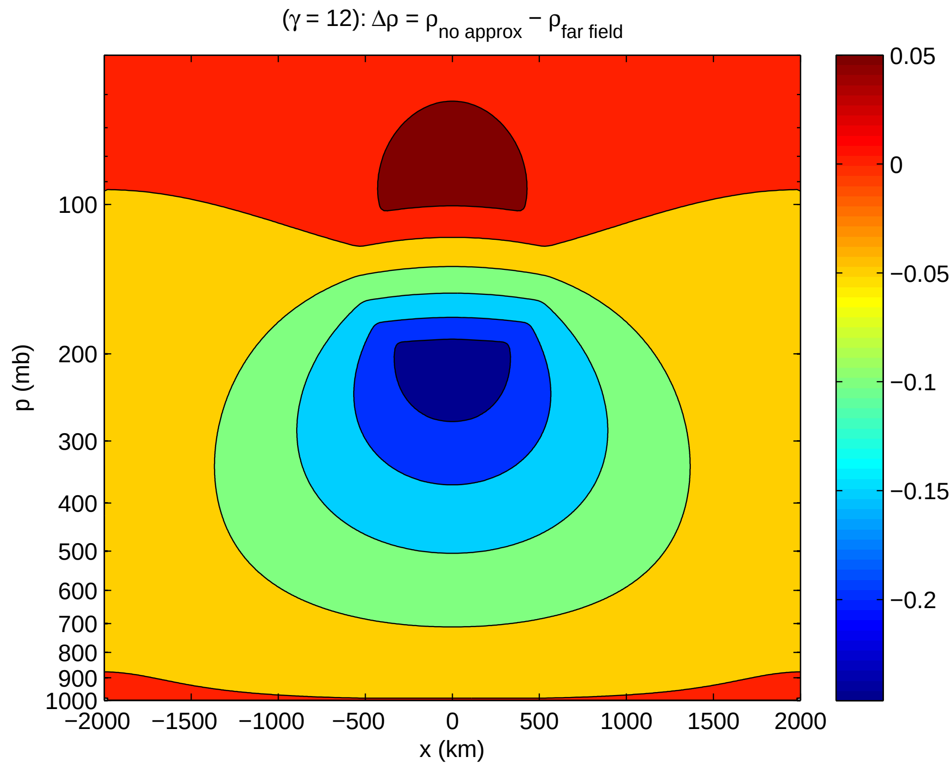

Figure 4.5: The difference of density (kg m^{-3}), the far-field density subtracted from the unapproximated density, for the case of a strong cyclone, $\gamma = 12$.

Qualitatively, the density approximated solutions do not have the upward flare of the jets seen in the unapproximated solutions. The reason for this behavior can be deduced from Figs. 4.5 and 4.6, which are plots of the difference in density and the difference in wind speed respectively, for a strong cyclone. Figure 4.5 shows that the density is underestimated in the upper half of the PV anomaly and surrounding region when it is approximated by the far-field density. Looking at the difference of v in Fig. 4.6 we see cyclonic flow in the upper region of the domain. Likewise, the approximated density is an over estimation of the true density in the lower region of the PV anomaly. From this an anticyclonic cirulation is seen in the lower region of the domain. Put together, the effect of the density from

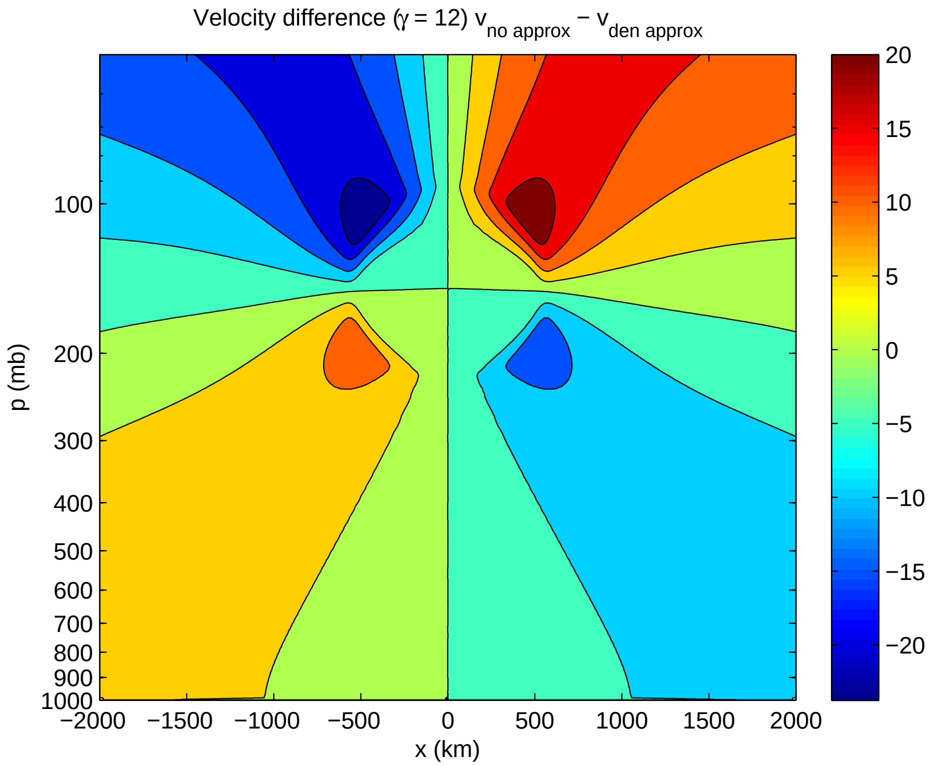

Figure 4.6: The difference of v (m s^{-1}), the v field with density approximated by the far-field density subtracted from the v field when density is unapproximated. For the case of a strong cyclone, $\gamma = 12$.

its approximated form is to shift the cyclonic circulation upwards creating the flare of the isotachs that is seen. For the anticyclone an analogous argument exists, and the anticyclonic circulation is seen to be shifted upwards as well.

4.5 Stratosphere

The model atmosphere of the analytical theory does not include a stratosphere. Here, by modifying our definition of the buoyancy frequency, we include a stratosphere. Recall the vertical profile of the analytical model was given by a buoyancy frequency that varied inversely with potential temperature, $N(\theta) = (N_c\theta_c)/\theta$, where N_c is a reference buoyancy frequency at θ_c. This definition captures the magnitude and general trend of a buoyancy frequency that decreases with height in the troposphere, as seen in Fig. 4.1. To add a stratosphere our new definition is

$$N(\theta) = \begin{cases} \frac{N_t\theta_t}{\theta}, & \text{for } \theta_B \le \theta < \theta_{tp} \\ \\ \frac{N_s\theta_s}{\theta}, & \text{for } \theta_{tp} \le \theta \le \theta_T, \end{cases} \tag{4.10}$$

where the N_t and N_s are reference values for the troposphere and stratosphere, and θ_{tp} denotes the tropopause potential temperature. This definition retains the decrease with height in the troposphere, has a discontinuous jump to higher values at the tropopause, then decreases with height again in the stratosphere.

The solutions with a stratosphere for the parameters $\theta_t = 350$ K, $N_t = 1.03 \times 10^{-2}$ s^{-1}, $\theta_{tp} = 380$ K, $\theta_s = 380$ K, and $N_s = 2.06 \times 10^{-2}$ s^{-1} are shown in in Fig. 4.7. The first thing to note is the higher gradient of potential temperature above $\theta = 380$ K. This region is characterized by increased static stability as well as increased potential vorticity, like the stratosphere of the real atmosphere. In terms of maximum wind speed the cyclones of the model with a stratosphere are higher, and this effect increases with intensity. The reason for this can be explained as follows. The ellipse of anomalous PV "pulls" the θ-contours towards it from above and below. When a stratosphere is present, the higher PV air directly above the ellipse is pulled downward, creating another PV anomaly due to a depression of the tropopause. This tropopause PV anomaly adds an additional cyclonic circulation—in the upper troposphere and stratosphere—to the cyclonic circulation generated by the ellipse anomaly. For a strong cyclone $\gamma = 12$, the maximum wind speed of the solutions with a stratosphere were 4 m s^{-1} faster.

For the anticyclone, an analogous situation occurs when the θ-contours bow outwards. Directly above the low PV anomaly the tropopause is pushed upwards making it slightly concave. This curvature of the tropopause generates an anticyclonic circulation in the stratosphere. The effect is weak and the additional circulation is in the higher regions of the domain so that the maximum wind speed is unaffected.

In this chapter we have constructed a numerical model based on the equations used for the analytical theory in Chapter 3. Solutions for this fully unapproximated model with

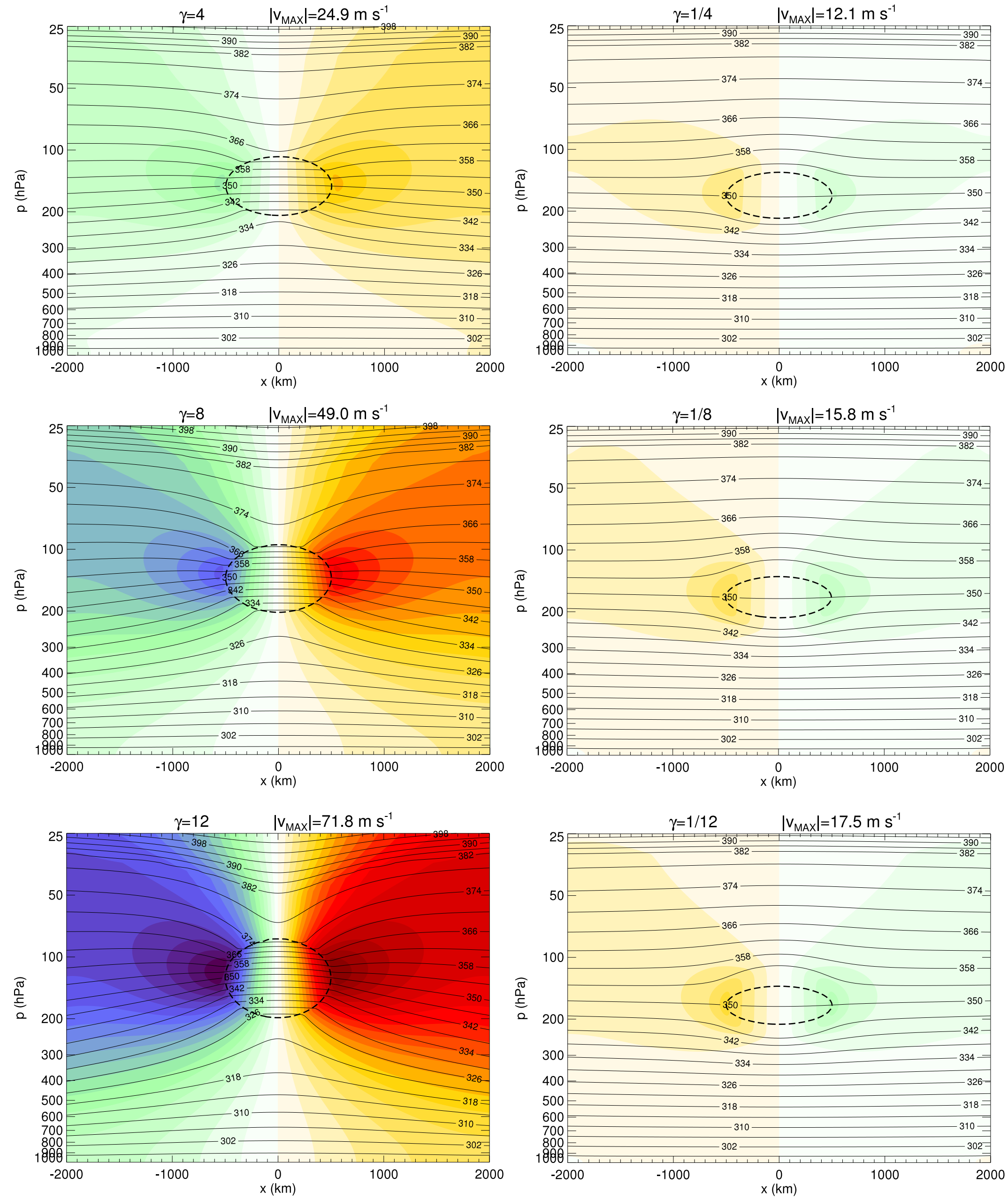

Figure 4.7: The conventions here are the same as in Fig. 4.3, though a stratosphere has been added by modifying the buoyancy frequency profile to that in given in (4.10).

no stratosphere were first presented. Next, we computed the solutions for the case when density is held at the far-field values. Comparing these solutions with the unapproximated solutions we found that for cyclones the unapproximated solutions had higher maximum windspeeds. For anticyclones the unapproximated solutions had lower maximum windspeeds. The jets in the density approximated solutions do not flare upwards like the jets in the unapproximated solutions. Lastly, we presented solutions for a model atmosphere with a stratosphere. Comparing the stratosphere solutions to the unapproximated solutions without a stratosphere, it was seen that for cyclones the maximum wind speeds were higher for the stratosphere solutions. For anticyclones the maximum wind speeds did not differ between the solutions.

Chapter 5

CONCLUSIONS

The main results of this work are the simple analytical solutions of the PV invertibility principle presented in Chapter 3. Isentropic coordinates were used to derive equations for the case of line symmetric, geostrophic flow. The solutions describe both the interior of a potential vorticity anomaly as well as the induced exterior flow. The solutions are valid for intrusions of high PV as well as those of low PV. The case of high PV intruding into low latitudes is of most interest, due to the association with features in the cloud field (moisture bursts, cloud surges) and in the flow field (TUTT's) which have important implications for transient convection in the tropics as well as aiding in tropical cyclone development. Some essential characteristics of the solutions for high PV are the upgliding isentropes and cyclonic circulation. In the case of low PV intrusions the isentropes were seen to bow outward from the PV anomaly and the circulation was anticyclonic.

Our line symmetric, geostrophic solutions (analytical) of the PV invertibility principle complement the circularly symmetric, geostrophic solutions (analytical) of Eliassen and Kleinschmidt Jr. (1957), and the circularly symmetric, gradient solutions (numerical) of Hoskins et al. (1985) and Thorpe (1986).

In Chapter 2 we surveyed reanalysis data from YOTC to validate our analytical theory. Time series of the 250 hPa potential vorticity over the North Pacific Basin for two winter seasons were created and an example of each type of intrusion was selected for closer study. Vertical cross-sections were then made displaying potential vorticity, the meridional wind, and isentropic surfaces. In the case of the high PV intrusion, cyclonic jets as well as upgliding isentropes were seen. For the case of the low PV intrusion, the circulation was anticyclonic and the isentropes bowed outwards. We conclude that qualitatively the PV intrusion events are in agreement with the idealized solutions.

In Chapter 4 an unapproximated version of the equations used in the analytical theory were solved numerically. Doing so allowed us to analyze the effect of approximating the density by the far-field density. When the density is not approximated the equation set is weakly nonlinear, whereas the form used in the analytical theory is linear. In terms of the maximum wind speed, the density approximated cyclones were slower by at most 3 m s^{-1}, and the anticyclones faster by 0.1 m s^{-1}. The unapproximated solutions were seen to have jets that flare upwards slightly. Based on these small differences we gained confidence in our use of this approximation.

Also, in the analytical theory a stratosphere is not present. In the numerical study a stratosphere was added. This was done by defining the buoyancy frequency to be a piecewise function of θ, with a reference value for the troposphere and a higher reference value for the stratosphere. With this definition there is a discontinuous jump in buoyancy frequency at the tropopause. This causes a jump in the background potential vorticity at the tropopause as well. Comparing the maximum wind speeds, the cyclones with a stratosphere were faster by at most 4 m s^{-1}, and the anticyclone speeds were unchanged. Based on these findings, and the simplicity gained by the analytical solutions, the neglect of the stratosphere is seen to be only a small compromise.

We conclude by suggesting some future work with the numerical model. Silvers and Schubert (2012) present their own numerical model based on inversion of potential vorticity which contains a lower boundary with topography as well as surface gradients of potential temperature. Coupling the two models could lead to an understanding of the flow field that results when an upper level PV anomaly interacts with elevated terrain. By using a potential temperature anomaly on the lower boundary to simulate a surface front, the model could be a useful tool for studying atmospheric rivers.

BIBLIOGRAPHY

Appenzeller, C., and H. Davies, 1992: Structure of stratospheric intrusions into the troposphere. *Nature*, **358**, 570–572.

Appenzeller, C., H. C. Davies, and W. A. Norton, 1996: Fragmentation of stratospheric intrusions. *J. Geophys. Res.*, **101**, 1435–1456.

Davis, C. A., and L. F. Bosart, 2004: The tt problem: Forecasting the tropical transition of cyclones. *Bull. Amer. Meteor. Soc.*, **85**, 1657–1662.

Dritschel, D. G., 1989: Contour dynamics and contour surgery: numerical algorithms for extended, high-resolution modelling of vortex dynamics in two-dimensional, inviscid, incompressible flows. *Comput. Phys. Rep.*, **10**, 78–146.

Durran, D. R., and D. B. Weber, 1988: An investigation of the poleward edges of cirrus clouds associated with midlatitude jet streams. *Mon. Wea. Rev.*, **116**, 702–714.

Eliassen, A., and E. Kleinschmidt Jr., 1957: *Dynamic Meteorology*. Handbuch der Physik, Vol. 30, Springer-Verlag, 154 pp.

ESRL/PSD, 2012: Atmospheric river information page. http://www.esrl.noaa.gov/psd/atmrivers/.

Fulton, S. R., and W. H. Schubert, 1985: Vertical normal mode transforms: theory and application. *Mon. Wea. Rev.*, **113**, 647–658.

Funatsu, B. M., and D. W. Waugh, 2008: Connections between potential vorticity intrusions and convection in the eastern tropical pacific. *J. Atmos. Sci.*, **65**, 987–1002.

Gill, A. E., 1981: Homogeneous intrusions in a rotating stratified fluid. *J. Fluid Mech.*, **103**, 275–295.

Gill, A. E., 1982: *Atmosphere-Ocean Dynamics*. International Geophysics Series, Vol. 30, Academic Press.

Griffiths, D. J., 1999: *Introduction to Electrodynamics*. Benjamin Cummings.

Hoskins, B. J., and T. Ambrizzi, 1993: Rossby wave propagation on a realistic longitudinally varying flow. *J. Atmos. Sci.*, **50**, 1661–1671.

Hoskins, B. J., M. E. McIntyre, and A. W. Robertson, 1985: On the use and significance of isentropic potential vorticity maps. *Quart. J. Roy. Meteor. Soc.*, **111**, 877–946.

Kelley, W. E., and D. R. Mock, 1982: A diagnostic study of upper tropospheric cold lows over the western north pacific. *Mon. Wea. Rev.*, **110**, 471–480.

Kiladis, G. N., 1998: Observations of Rossby waves linked to convection over the eastern tropical pacific. *J. Atmos. Sci.*, **55**, 321–339.

Kiladis, G. N., and K. M. Weickmann, 1992: Extratropical forcing of tropical pacific convection during northern winter. *Mon. Wea. Rev.*, **120**, 1924–1938.

Knippertz, P., 2007: Tropical-extratropical interactions related to upper-level troughs at low latitudes. *Dynam. Atmos. Oceans*, **43**, 36–62.

McDowell, S. E., and H. T. Rossby, 1978: Mediterranean water: An intense mesoscale eddy off the bahamas. *Science*, **202**, 1085–1087.

McGuirk, J. P., A. H. Thompson, and N. R. Smith, 1987: Moisture bursts over the tropical pacific ocean. *Mon. Wea. Rev.*, **115**, 787–798.

Neiman, P. J., L. J. Schick, F. M. Ralph, M. Hughes, and G. A. Wick, 2011: Flooding in western washington: The connection to atmospheric rivers. *J. Hydrometeor.*, **12**, 1337–1358.

Newell, R. E., Y. Zhu, W. G. Read, and J. W. Waters, 1997: Relationship between tropical upper tropospheric moisture and eastern tropical pacific sea surface temperature at seasonal and interannual time scales. *Geophys. Res. Lett.*, **24**, 25–28.

Postel, G. A., and M. H. Hitchman, 1999: A climatology of Rossby wave breaking along the subtropical tropopause. *J. Atmos. Sci.*, **56**, 359–373.

Prater, M. D., and H. T. Rossby, 2000: The double irony of the meddy. *Maritimes (University of Rhode Island Marine Programs)*, **42**, No. 3.

Sadler, J. C., 1976: A role of the tropical upper tropospheric trough in early season typhoon development. *Mon. Wea. Rev.*, **104**, 1266–1278.

Sadler, J. C., 1978: Mid-season typhoon development and intensity changes and the tropical upper tropospheric trough. *Mon. Wea. Rev.*, **106**, 1137–1152.

Scott, R. K., J.-P. Cammas, P. Mascart, and C. Stolle, 2001: Stratospheric filamentation into the upper tropical troposphere. *J. Geophys. Res.*, **106**, 11,835–11,848.

Silvers, L. G., and W. H. Schubert, 2012: A theory of topographically bound balanced motions and application to atmospheric low-level jets. *J. Atmos. Sci.*, **69**, in press.

Thorpe, A. J., 1986: Synoptic scale disturbances with circular symmetry. *Mon. Wea. Rev.*, **114**, 1384–1389.

Waugh, D. W., and B. M. Funatsu, 2003: Intrusions into the tropical upper troposphere: Three-dimensional structure and accompanying ozone and OLR distributions. *J. Atmos. Sci.*, **60**, 637–653.

Waugh, D. W., and L. M. Polvani, 2000: Climatology of intrusions into the tropical upper troposphere. *Geophys. Res. Lett.*, **27**, 3857–3860.

Whitfield, M. B., and S. W. Lyons, 1992: An upper-tropospheric low over texas during summer. *Wea. Forecasting*, **7**, 89–106.

Wirth, V., 2000: Thermal versus dynamical tropopause in upper-tropospheric balanced flow anomalies. *Quart. J. Roy. Meteor. Soc.*, **126**, 299–317.

Appendix A

ELLIPTICAL COORDINATES

We make use of elliptical coordinates in the plane. The two different cases are referred to as the thin and thick lens. The semi-major axis lies in the horizontal position for the thin lens, and in the vertical for the thick lens.

A.1 Thin lens

The relationship between cartesian coordinates (x, z) and elliptical coordinates (ϱ, φ) is

$$x + iz = c\cosh(\varrho + i\varphi),$$

where $c = \left(a^2 - b^2\right)^{1/2}$ for semi-major axis a and semi-minor axis b. Alternatively, the relationship between these two coordinates can written in terms of the real and imaginary components as

$$x = c\cosh(\varrho)\cos(\varphi), \tag{A.1}$$

$$z = c\sinh(\varrho)\sin(\varphi). \tag{A.2}$$

From here we can easily construct coordinate curves of (ϱ, φ) in the plane. Squaring and adding (A.1) and (A.2) gives

$$\frac{x^2}{c^2\cosh^2(\varrho)} + \frac{z^2}{c^2\sinh^2(\varrho)} = 1,$$

which is the equation for an ellipse in the (x, z)-plane with semi-axes given by $a = c\cosh(\varrho)$ and $b = c\sinh(\varrho)$. Taking different values of ϱ over the range $0 \leq \varrho < \infty$ gives a family of ellipses. Now squaring (A.1) and (A.2) and taking their difference gives

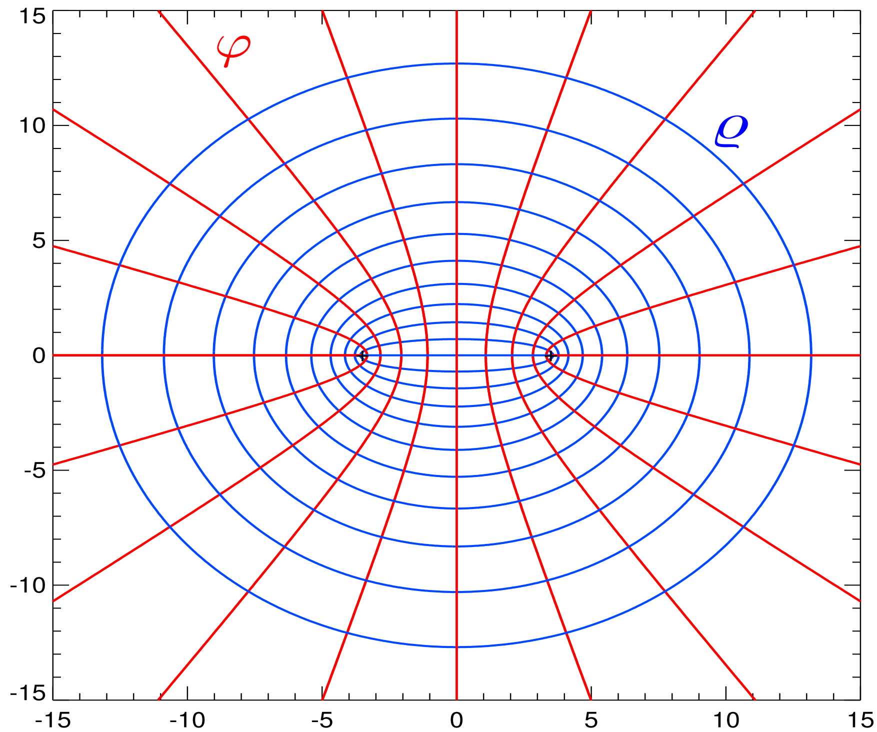

Figure A.1: Elliptic coordinates (ϱ, φ), as defined in (A.1) and (A.2) for the thin lens case. Lines of constant ϱ (blue) are the ellipses and lines of constant φ (red) are the hyperbolas. Both sets of curves have the same foci, located at $(x, z) = (\pm c, 0)$ and indicated by the $+$ symbols. Far from the origin, lines of constant ϱ are very nearly circles and lines of constant φ are very nearly straight radials. The units on the axes are kilometers, and only select values of ϱ and φ are shown for clarity.

$$\frac{x^2}{c^2 \cos^2(\varphi)} - \frac{z^2}{c^2 \sin^2(\varphi)} = 1.$$

This is the equation for hyperbolae with semi-major axis $a = c \cos(\varphi)$ and semi-minor axis $b = c \sin(\varphi)$. Varying φ over the range $0 \leq \varphi \leq 2\pi$ gives a family of hyperbolas. These families of ellipses and hyperbolas share the same foci at $(x, z) = (\pm c, 0)$, so are said to be confocal coordinates. See Fig. A.1. As ϱ becomes very large, $\cosh \varrho \approx \sinh \varrho \approx \frac{1}{2} e^{\varrho}$, so that the lines of constant ϱ approach circles with radius $\frac{1}{2} c e^{\varrho}$ in (x, z)-space, and the lines of constant φ approach the straight radials $\varphi = \tan^{-1}(z/x)$.

A.2 Thick lens

In this case (x, z) are related to (ϱ, φ) by

$$x + iz = c \sinh (\varrho + i\varphi) \, ,$$

where $c = \left(b^2 - a^2\right)^{1/2}$ for semi-major axis b and semi-minor axis a. Written in terms of real and imaginary parts

$$x = c \sinh (\varrho) \cos (\varphi) \, , \tag{A.3}$$

$$z = c \cosh (\varrho) \sin (\varphi) \, . \tag{A.4}$$

From (A.3) and (A.4) familys of ellipses and hyperbolas can be constructed in the exact same way as shown in the thin lens case.

Appendix B

NUMERICAL INTEGRATION

This section details the iterative method for solving the discretized (finite difference) version of the invertibility principle. The continuous formulation of the problem is given in Chapter 4 by (4.2)–(4.6). To discretize this set of equations we introduce the grid points $(x_j, \theta_k) = (-L + j\Delta x, \theta_B + k\Delta\theta)$ with $j = 0, 1, ..., J$ and $k = 0, 1, ..., K$, where $\Delta x = 2L/(J-1)$ and $\Delta\theta = (\theta_T - \theta_B)/(K-1)$. We then seek an approximate solution with gridpoint values $M_{j,k}$ satisfying the discretized form of (4.2)

$$A_{j,k}\left[(f\Delta x)^2 + M_{j-1,k} - 2M_{j,k} + M_{j+1,k}\right] + M_{j,k-1} - 2M_{j,k} + M_{j,k+1} = 0, \tag{B.1}$$

where the dimensionless coefficient $A_{j,k}$ is defined by

$$A_{j,k} = \frac{g\,(\Delta\theta)^2}{f\theta_k\rho_{j,k}P_{j,k}\,(\Delta x)^2}. \tag{B.2}$$

The density, given in (4.3), is discretized by centered difference as

$$\rho_{j,k} = \frac{p_0}{R\theta_k}\left(\frac{M_{j,k+1} - M_{j,k-1}}{c_p 2\Delta\theta}\right)^{(1-\kappa)/\kappa}. \tag{B.3}$$

Lastly, the discretized boundary condition (4.5) is given by

$$M_{j,K} = M_{j,K-1} + \Pi_T\Delta\theta \tag{B.4}$$

and (4.6) by

$$M_{j,0} = \left(\frac{1}{1+\frac{\Delta\theta}{\theta_B}}\right)M_{j,1}. \tag{B.5}$$

To solve (B.1) by successive over-relaxation we introduce the residual $(r_{j,k})$ for a particular iteration ν as

$$A^{\nu}_{j,k}\left[(f\Delta x)^2 + M^{\nu+1}_{j-1,k} - 2M^{\nu}_{j,k} + M^{\nu}_{j+1,k}\right] + M^{\nu+1}_{j,k-1} - 2M^{\nu}_{j,k} + M^{\nu}_{j,k+1} = r^{\nu}_{j,k}. \quad \text{(B.6)}$$

The Montgomery potential for the current iteration $(\nu + 1)$ is related to the Montgomery potential and residual of the previous iteration (ν) by

$$M^{\nu+1}_{j,k} = M^{\nu}_{j,k} + \frac{\omega r^{\nu}_{j,k}}{2\left(1 + A^{\nu}_{j,k}\right)}, \quad \text{(B.7)}$$

where ω is the over-relaxation factor. The optimum value for ω was determined experimentally (see Fig. B.1) to be 1.98 for a 200×150 grid. For the figures shown in Chapter 4 we

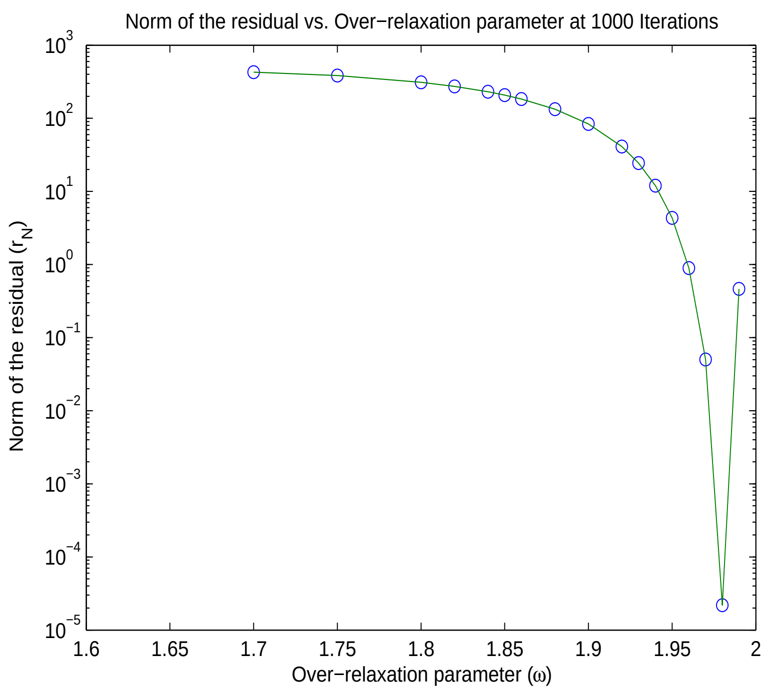

Figure B.1: The norm of the residual at 1000 iterations on a grid of 200 points (horizontal) by 150 points (vertical) is plotted for various values of the over-relaxation parameter (ω) between $1.7 \leq \omega < 2$. The value of $\omega = 1.98$ was found to maximize convergence in this case.

used a grid with $J = 400$ and $K = 300$ for the domain $-2000 \leq x \leq 2000$ and $295 \leq \theta \leq 415$ K.

A summary of the solution procedure is as follows. Equations (B.6) and (B.7) are iterated on the interior of the domain starting with the initial estimate of $M_{j,k} = \tilde{M}(\theta)$. The density (B.3) and the dimensionless coefficient (B.2) are updated each iteration as well. On the lateral boundaries M is held at the far-field value $\tilde{M}$, while the upper (B.4) and lower (B.5) boundary conditions are enforced at each step. In order to gauge the convergence rate, we have monitered the norm of the residual as the iteration proceeds. The results shown have been iterated until the norm of the residual is less than 10^{-5}. The above process determines the Montgomery potential in the entire domain for a given $\tilde{M}(\theta)$. From the Montgomery potential, the wind field can be recovered using geostrophic balance, and the pressure field can be computed using hydrostatic balance.